nature neuroscience

Article

https://doi.org/10.1038/s41593-024-01619-1

Messenger RNA transport on lysosomal vesicles maintains axonal mitochondrial homeostasis and prevents axonal degeneration

Received: 16 May 2023

Accepted: 7 March 2024

Published online: 10 April 2024

Check for updates

Raffaella De Pace[1,5], Saikat Ghosh[1,5], Veronica H. Ryan[2], Mira Sohn[3], Michal Jarnik[1], Paniz Rezvan Sangsari[4], Nicole Y. Morgan[4], Ryan K. Dale[3], Michael E. Ward[2] & Juan S. Bonifacino[1]

In neurons, RNA granules are transported along the axon for local translation away from the soma. Recent studies indicate that some of this transport involves hitchhiking of RNA granules on lysosome-related vesicles. In the present study, we leveraged the ability to prevent transport of these vesicles into the axon by knockout of the lysosome–kinesin adaptor BLOC-one-related complex (BORC) to identify a subset of axonal mRNAs that depend on lysosome-related vesicles for transport. We found that BORC knockout causes depletion of a large group of axonal mRNAs mainly encoding ribosomal and mitochondrial/oxidative phosphorylation proteins. This depletion results in mitochondrial defects and eventually leads to axonal degeneration in human induced pluripotent stem cell (iPSC)-derived and mouse neurons. Pathway analyses of the depleted mRNAs revealed a mechanistic connection of BORC deficiency with common neurodegenerative disorders. These results demonstrate that mRNA transport on lysosome-related vesicles is critical for the maintenance of axonal homeostasis and that its failure causes axonal degeneration.

Lysosomes are membrane-bound, acidic organelles that are primarily involved in macromolecular degradation but also play roles in other processes, including nutrient signaling and gene regulation[1,2]. Lysosomes are highly heterogeneous in size, shape, pH, acid hydrolase content and overall composition, reflecting different maturational states or specialized functions. Additionally, they share luminal and/or membrane components with late endosomes and various lysosome-related organelles. To encompass this diversity, herein we collectively refer to all these organelles as 'lysosome-related vesicles'. Axonal lysosome-related vesicles are a prime example of such heterogeneity[3,4]. In the axon, lysosome-related vesicles move bidirectionally along microtubule tracks[5–13]. Movement toward the distal axon (that is, anterograde transport) is dependent on coupling to kinesin motor proteins, whereas movement toward the soma (that is, retrograde transport) is dependent on coupling to the dynein–dynactin motor complex[3,4]. In general, anterograde lysosome-related vesicles are

[1]Neurosciences and Cellular and Structural Biology Division, Eunice Kennedy Shriver National Institute of Child Health and Human Development, National Institutes of Health, Bethesda, MD, USA. [2]Neurogenetics Branch, National Institute of Neurological Disorders and Stroke, National Institutes of Health, Bethesda, MD, USA. [3]Bioinformatics and Scientific Programming Core, Eunice Kennedy Shriver National Institute of Child Health and Human Development, National Institutes of Health, Bethesda, MD, USA. [4]Biomedical Engineering and Physical Science Shared Resource, National Institute of Biomedical Imaging and Bioengineering, National Institutes of Health, Bethesda, MD, USA. [5]These authors contributed equally: Raffaella De Pace, Saikat Ghosh. e-mail: juan.bonifacino@nih.gov

smaller and less acidic than retrograde lysosome-related vesicles[5,12–14]. Moreover, at least some anterograde lysosome-related vesicles contain *trans*-Golgi network (TGN) and endosomal and synaptic vesicle proteins, suggesting that they serve as biosynthetic carriers or lysosome precursors[9,13]. The population of retrograde lysosome-related vesicles includes mature lysosomes, late endosomes, autolysosomes (fusion of lysosomes with autophagosomes) and/or amphisomes (fusion of lysosomes with late endosomes)[15–18]. The distinct properties of anterograde and retrograde lysosome-related vesicles suggest that these organelles undergo maturation in the distal axon.

Although anterograde lysosome-related vesicles most likely serve as precursors for mature lysosomes, they could perform additional functions along the way. One such function has recently come to light, with the discovery that RNA granules hitchhike on lysosome-related vesicles for long-distance transport along the axon[19]. RNA granules are phase-separated condensates of RNAs and RNA-binding proteins (RBPs) that enable regulation of RNA functions in various post-transcriptional processes[20]. RNA granules coupled to lysosome-related vesicles in the axon carry both miRNAs[21,22] and mRNAs[19] for regulated local translation at sites distal from the soma. Moreover, axonal late endosomes serve as platforms for local translation of nuclear-encoded mitochondrial mRNAs by associated ribosomes[23]. RBPs and mRNAs can also undergo axonal transport in association with mitochondria[24,25] and early endosomes[23,26] or through direct binding of RBPs to microtubule motors[27–29]. It is currently unknown whether each of these modalities is responsible for the transport of different subsets of RNAs.

Interrogating the role of axonal lysosome-related vesicles in RNA transport requires a method to halt movement of lysosome-related vesicles without altering other transport mechanisms. This discrimination would not be possible by silencing the motor proteins themselves, as this would have widespread effects on axonal transport. Instead, a more precise approach would be to silence a specific adaptor of lysosomes to kinesins. An adaptor system meeting this requirement is an ensemble of the BLOC-one-related complex (BORC), the small GTPase ARL8 and the adaptor protein PLEKHM2 (also known as SKIP), which mediates coupling of lysosomes to kinesins 1 and 3 (refs. 30–32) (Fig. 1a). BORC is a hetero-octameric protein complex composed of subunits named BORCS1–8 (ref. 31). Knockout (KO) of individual BORC subunits impairs anterograde transport of lysosome-related vesicles and causes their depletion from the peripheral cytoplasm in non-neuronal cells and from the axon in neurons[6,7,11,31]. These effects are specific, as the cytoplasmic or axonal distributions of other organelles, such as mitochondria and synaptic vesicles, are not affected[11,31]. Moreover, BORC-subunit KOs cause neonatal death in mice[7,11], and hypomorphic mutations are associated with severe neurodevelopmental/neurodegenerative phenotypes in both mice[7] and humans[33–35]. These findings indicate that BORC-dependent transport of lysosome-related vesicles is particularly critical for the development and function of the central nervous system (CNS).

In the present study, we leveraged the ability to prevent the transport of lysosome-related vesicles into the axon by KO of BORC subunits to examine the impact of this manipulation on the repertoire of mRNAs, the transport of specific mRNAs and the impact on other organelles in the axon. We found that KO of BORC subunits in human neurons derived from induced pluripotent stem cells (iPSCs) led to a substantial reduction in lysosome-related vesicles and a depletion of a large subset of mRNAs in the axon. Most prominent among the depleted mRNAs were those encoding components of ribosomes and of the mitochondrial oxidative phosphorylation system (OXPHOS). This resulted in decreased protein translation and mitochondrial abnormalities. Moreover, the depleted mRNAs were associated with pathways of neurodegeneration in Parkinson's, Alzheimer's, Huntington's and prion diseases and in amyotrophic lateral sclerosis (ALS). These findings indicate that hitchhiking on lysosome-related vesicles is a major pathway for the transport of mRNAs into the axon and that this process is critical for the maintenance of mitochondrial homeostasis. In addition, our findings reveal a plausible mechanism for axonal degeneration in humans with mutations in BORC subunits that is related to the pathogenesis of common neurodegenerative disorders.

Results

BORC-KO depletes axonal lysosome-related vesicles

To investigate the role of axonal transport of lysosome-related vesicles in mRNA transport and axonal homeostasis, we used human iPSCs expressing the neuronal transcriptional activator neurogenin 2 (NGN2) under the control of a doxycycline-inducible promoter[36,37]. Culture of these iPSCs in doxycycline-containing medium induces their differentiation into cortical-like, glutamatergic neurons (termed i3Neurons)[36,37] (Fig. 1b). We used CRISPR–Cas9 to KO the genes encoding the BORCS5 (also known as myrlysin) or BORCS7 (also known as lyspersin) subunit of BORC[31] in these iPSCs and stable lentiviral re-expression of BORCS5 or BORCS7, respectively, in the KO iPSCs (Fig. 1c). Immunofluorescence microscopy of wild-type (WT) i3Neurons cultured on glass coverslips for 25 d showed that they had distinct soma and dendrites labeled for the somatodendritic marker MAP2 and axons labeled for the synaptic vesicle marker SYP (Fig. 1d; WT). The axonal domain was extensively developed at this time, appearing as a lace-like network on the coverslips. Lysosomal vesicles were most concentrated in the soma, but they were also apparent as fine puncta in the dendrites and axons, as detected by staining for the lysosomal proteins LAMP1 or LAMTOR4 (Fig. 1e; WT).

BORCS5 or BORCS7 KO (referred to as BORC-KO) did not prevent the differentiation of the iPSCs into i3Neurons. Additionally, the neurons had well-defined somatodendritic and axonal domains (Fig. 1d). Furthermore, these KOs had no effect on the presence of synaptic vesicles labeled for SYP and mitochondria labeled for TOMM20 in the axon (Fig. 1d). Also unaffected were the distributions of TGN or endosomal markers, such as CI-MPR, EEA1 and TGN46

Fig. 1 | Depletion of axonal lysosomes in BORCS5-KO and BORCS7-KO i3Neurons. a, Schematic representation of the coupling of lysosomes to the plus-end-directed kinesin-1 motor through the BORC–ARL8–PLEKHM2 ensemble[31]. **b**, iPSCs were differentiated for 3 d in DMEM/F12 medium supplemented with NEAAs, GlutaMAX and N2A and doxycycline (DOX) and further cultured for 25–45 d in BrainPhys medium containing B27, laminin, BDNF, NT-3 and DOX. **c**, SDS-PAGE and immunoblot (IB) analysis of WT, BORCS5-KO, BORCS7-KO, BORCS5-KO re-expressing BORCS5-P2A-GFP (rescue) and BORCS7-KO re-expressing BORCS7-HA-P2A-GFP (rescue) iPSCs using antibodies to BORCS5, BORCS7 and GAPDH (loading control). After self-cleavage, 22 amino acid residues at the N-terminus of P2A remain linked to the upstream protein, thus the higher molecular mass in the rescue cells. The positions of molecular mass markers (in kDa) are indicated on the left. **d**,**e**, i3Neurons derived from the WT, BORCS5-KO, BORCS7-KO (**d**) and BORCS5 rescue and BORCS7 rescue (**e**) iPSCs shown in **c** were cultured for 25 d on glass coverslips and immunostained for endogenous MAP2 (soma and dendrites) (magenta), synaptophysin (SYP) (synaptic vesicles), TOMM20 (mitochondria), LAMP1 (lysosomes) or LAMTOR4 (lysosomes) (all grayscale). Nuclei were stained with DAPI (blue). Scale bars, 10 µm. See also Extended Data Figs. 1, 2a and 8a. Panel **e** additionally shows higher intensity images of MAP2 staining in grayscale (MAP2 bright). **f**, Quantification of the number of axonal puncta staining for LAMP1 or LAMTOR4 in various i3Neuron lines relative to WT i3Neurons (defined as 1.0) from $n = 3$ independent experiments such as that shown in **e**. Results are represented as SuperPlots[77] showing the individual data points in different colors, the mean from each experiment and the mean of the means ± s.d. Statistical significance was calculated by one-way ANOVA with Dunnett's multiple comparisons test. Axonal LAMP1 significance versus WT: BORCS5 KO ***$P < 0.001$, BORCS7 KO ***$P < 0.001$, BORCS5 rescue $P = 0.995$ and BORCS7 rescue $P = 0.157$. Axonal LAMTOR4 significance versus WT: BORCS5 KO ***$P < 0.001$, BORCS7 KO ***$P < 0.001$, BORCS5 rescue ***$P < 0.001$ and BORCS7 rescue $P = 0.870$. NS, not significant, relative to WT.

https://doi.org/10.1038/s41593-024-01619-1

(Extended Data Fig. 1). In contrast, BORCS5 or BORCS7 KO caused a marked depletion of lysosome-related vesicles from the axon (Fig. 1e,f and Extended Data Fig. 2a,b). The presence of axons in the fields devoid of LAMP1 was evidenced by SYP and TOMM20 staining (Fig. 1d) and by increasing the brightness of the MAP2 channel (Fig. 1e; MAP2 bright). Stable re-expression of BORCS5 or BORCS7 in the corresponding KO cells restored the presence of lysosome-related vesicles in the axon (Fig. 1e,f and Extended Data Fig. 2a,b). These experiments thus

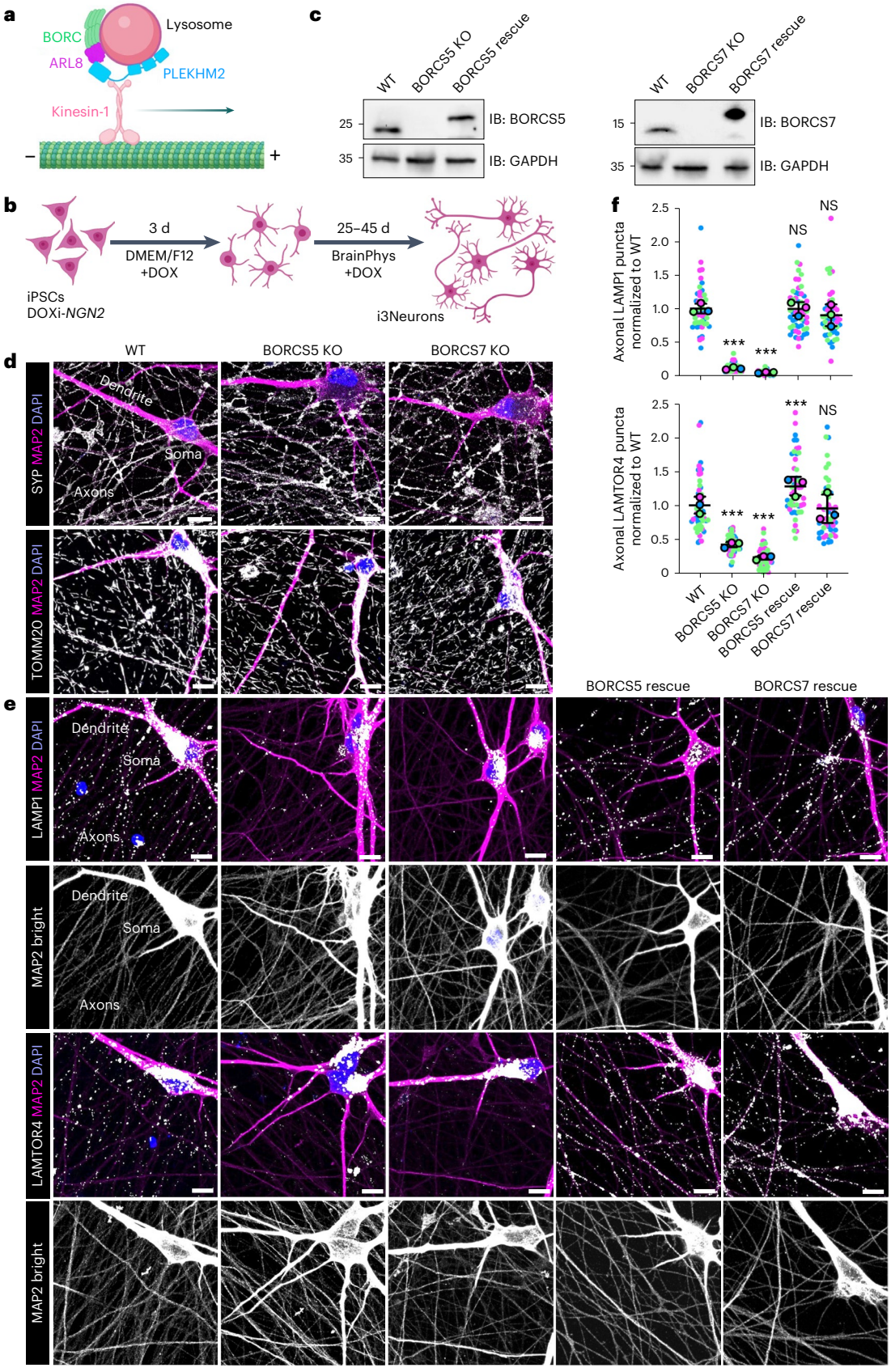

demonstrated that BORC-KO specifically depleted lysosome-related vesicles from the axon of human i3Neurons, as previously shown for silencing of BORC subunits in rat and mouse hippocampal and cortical neurons[6,7,11].

Axonal enrichment of ribosomal and mitochondrial protein mRNAs

To analyze the mRNA profile in the axon of WT and BORC-KO i3Neurons, we built a microfluidic device that allows isolation of sufficient axonal material for transcriptomic analyses (Fig. 2a,b and Extended Data Fig. 3a,b). The iPSCs were plated on the two side chambers, and, upon differentiation into i3Neurons, only axons were thin and long enough to grow into the middle chamber (Fig. 2a,b). Immunofluorescence microscopy of WT i3Neurons grown for 45 d showed that the middle chamber contained numerous axons staining for the microtubule-associated protein Tau (Extended Data Fig. 3c), the synaptic vesicle protein SV2, the mitochondrial protein TOMM20 and the lysosomal protein LAMP1 but not the somatodendritic marker MAP2 and the axon initial segment (AIS) protein ankyrin G (ANKG) (Fig. 2c and Extended Data Fig. 3c). The side chambers stained for all these markers as well as the nuclear DNA dye DAPI (Fig. 2c and Extended Data Fig. 3c). Therefore, the middle chamber contained pure axons, whereas the two side chambers contained all neuronal domains, including axons and the AIS. On this basis, we refer to preparations from these chambers as 'axons' and 'neurons', respectively. Immunoblot analysis of these preparations confirmed enrichment of the synaptic vesicle protein SYN1 and depletion of MAP2 relative in the axon relative to the neurons (Fig. 2d).

We performed RNA sequencing (RNA-seq) and differential expression analysis in axon and neuron preparations from day-45 i3Neurons (Fig. 2e–h and Supplementary Tables 1 and 2). These analyses identified transcripts from an average of 11,089 axonal and 29,410 neuronal genes in WT and 16,867 axonal and 31,211 neuronal genes in BORCS5-KO i3Neurons (Fig. 2e). In WT axons, 61% of the RNA counts corresponded to mitochondrial ribosomal RNAs (mt rRNAs) and 38% to protein-coding mRNAs (Fig. 2f). In WT neurons, on the other hand, over 98% of the RNAs were protein coding (Fig. 2f). The abundance of mt rRNAs in the axon was previously reported for embryonic mouse and human motor neurons and likely reflects the enrichment of mitochondria in axons[38–41]. A large subset of protein-coding transcripts (1,628 genes) was significantly more abundant in WT axons relative to WT neurons (Fig. 2g). Among the most enriched transcripts in WT axons were mitochondria-encoded mRNAs for OXPHOS proteins (ND1, ND4 and COX1) and nuclear-encoded mRNAs for ribosomal proteins (RPL12, RPL26, RPL31 and RPS18) (Fig. 2g and Supplementary Tables 1 and 2). Gene Ontology (GO) Cellular Component analysis of all axon-enriched transcripts in WT neurons showed enrichment in mRNAs for ribosomal and mitochondrial proteins, both nuclear encoded and mitochondria encoded (Fig. 2h), as previously reported for other axonal or nerve terminal preparations[38,40–44]. In contrast, the neuron fraction was most enriched in mRNAs coding for chromosomal and nuclear proteins (Fig. 2h).

BORC-KO depletes axonal mRNAs for ribosomal and OXPHOS proteins

Next, we evaluated the impact of depleting axonal lysosome-related vesicles on the repertoire of axonal mRNAs. We observed a decrease in the proportion of axonal mt rRNAs in BORCS5 KO (26%) relative to WT i3Neurons (61%) (Fig. 2f). Comparison of specific protein-coding mRNAs in WT versus BORCS5-KO axons revealed that BORCS5 KO resulted in a marked decrease in a subset of mRNAs (2,230 genes) (Fig. 3a). Many of these mRNAs corresponded to those that are normally enriched in the axon (Fig. 2g and Supplementary Tables 1 and 2)[38–42], as exemplified by those shown in Fig. 3b.

GO Cellular Component and KEGG functional enrichment analyses showed that the most significant terms of axonal mRNAs depleted in BORCS5-KO i3Neurons corresponded to those encoding ribosomal and mitochondrial proteins (Fig. 3c,d). KEGG also showed that 6 of the top 12 terms corresponded to neurodegenerative disorders (Parkinson's disease, Huntington's disease, prion disease, pathways of neurodegeneration–multiple diseases, ALS and Alzheimer's disease) (Fig. 3d), suggesting a common mechanism of axonal pathology in BORC-deficient neurons and neurodegenerative disorders. All these disorders, as well as diabetic cardiomyopathy, thermogenesis and reactive oxygen species (ROS), share a relationship to OXPHOS (Fig. 3d,e). The mRNAs depleted in BORCS5-KO axons and related to common neurodegenerative disorders include both nuclear-encoded and mitochondria-encoded mRNAs for components of electron transport chain complexes, proteasome subunits and kinesin-1 heavy chains (Extended Data Fig. 4a and Supplementary Table 2). They also include mRNAs for proteins that are mutated in neurodegenerative disorders (Extended Data Fig. 4a and Supplementary Table 2). The ribosome category, on the other hand, shows a relationship to coronavirus disease 2019 (COVID-19) (Fig. 3e, Extended Data Fig. 4b and Supplementary Table 2). This category includes transcripts for both cytoplasmic and mitochondrial ribosomes, with only the former relating to COVID-19 (Extended Data Fig. 4b and Supplementary Table 2). These results are consistent with a defect in the transport of specific populations of nuclear-encoded mRNAs into the axon and with a reduction in transcription or stability of mitochondria-encoded mRNAs.

BORCS5 KO also caused a relative increase in a different subset of mRNAs (3,533 genes) (Fig. 3a). In contrast to the predominance of a few GO categories, such as mitochondria and ribosomes among the depleted mRNAs in BORCS5-KO i3Neurons, the increased mRNAs belonged to diverse categories, including chromosomes, mitotic

Fig. 2 | Axonal mRNA profile of i3Neurons cultured in a microfluidic device. **a**, Schematic representation of a microfluidic device designed to isolate pure axons. The device is composed of three chambers separated by two sets of microgrooves. i3Neurons were plated on the two side chambers (green) and cultured for 45 d, during which time axons grew toward the central chamber (pink). **b**, Phase-contrast image of neurons and axons grown in the microfluidic device. **c**, i3Neurons grown in the microfluidic device were immunostained for the indicated proteins (all grayscale and/or magenta). Nuclei were stained with DAPI (blue). The experiment was repeated three times. Scale bars, 20 µm. **d**, Immunoblot analysis of protein extracts from neuronal and axonal compartments of the microfluidic device. The immunoblot was repeated two times. The positions of molecular mass markers (in kDa) are indicated on the left. **e**, RNA extracted from the axonal and neuronal compartments of $n = 2$ WT and $n = 3$ BORCS5 KO independent cultures of i3Neurons was subjected to RNA-seq. The number of genes with non-zero read counts was counted without normalization across the biological replicates. Box plots show the individual data points, median (center line indicating the 50th percentile), 75th percentile (top of the box) and 25th percentile (bottom of the box). The whiskers extend to the maximum and minimum data value that is no more than 1.5 times the interquartile range above or below the hinge. **f**, Proportion of the indicated RNA biotypes in axonal and neuronal preparations. **g**, MA plot of protein-coding genes in WT axons compared to WT neurons. Each dot represents a protein-coding gene with its mean normalized read count in $\log_{10}$ scale (x axis) and fold change in $\log_2$ scale (y axis). Insignificant (FDR > 0.1), significant (FDR < 0.1) and top 20 (lowest FDR) protein-coding DEGs for both up or down DEGs are colored gray, black and red, respectively. Top 20 gene names are indicated. **h**, Dot plots for GO Cellular Component gene sets enriched in WT axons versus WT neurons in RNA-seq. Enriched gene sets were arranged by statistical significance (FDR). The z-score captures both the direction of changes and the number of genes changing in each direction. A larger absolute z-score indicates a more biased direction toward increase or decrease. Statistical significance was calculated by one-sided Fisher's exact test. P values were adjusted for multiple comparisons using the Benjamini–Hochberg method.

https://doi.org/10.1038/s41593-024-01619-1

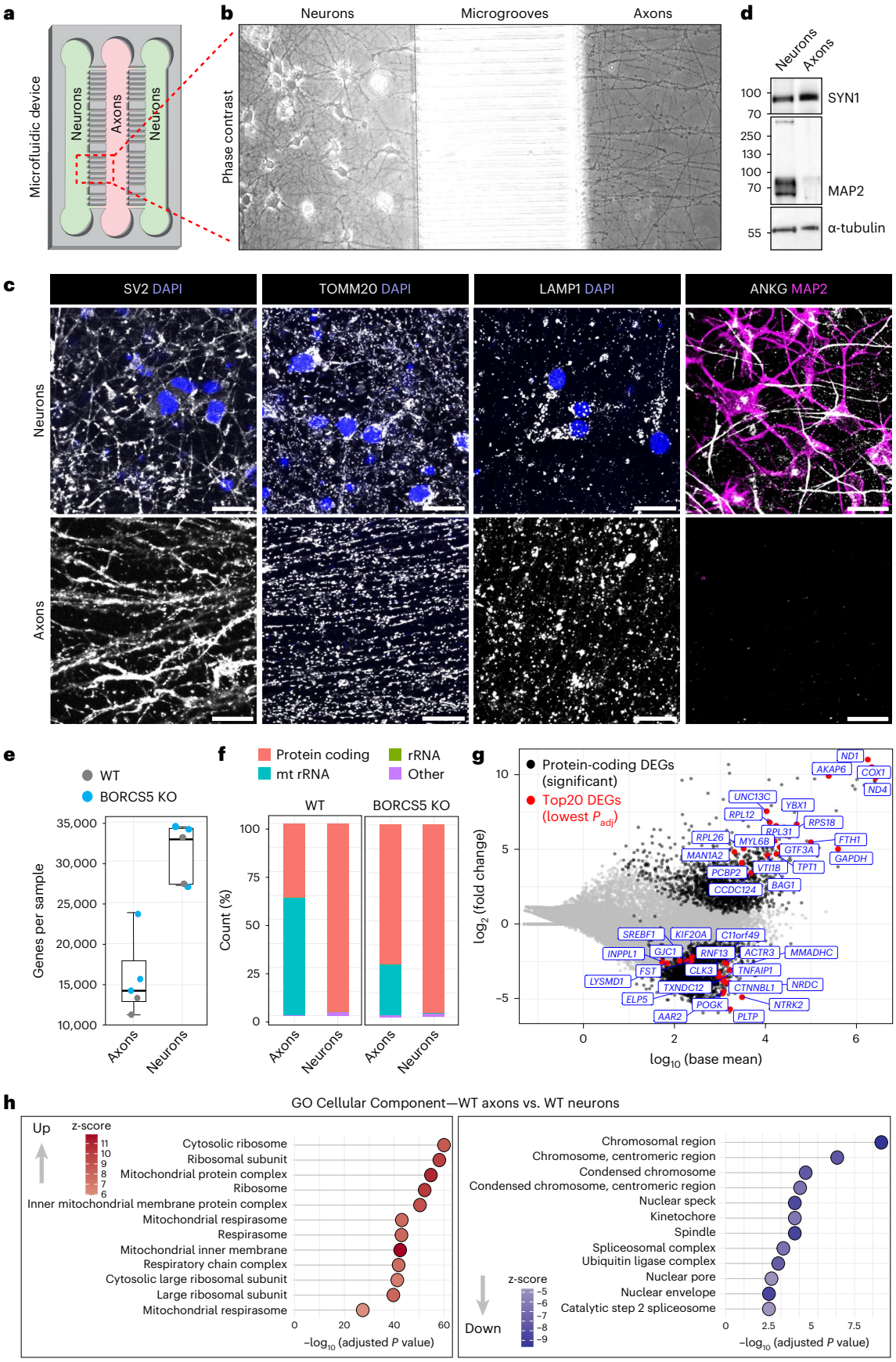

spindle, endoplasmic reticulum, nuclear envelope and focal adhesion (Fig. 3c), which also correspond to mRNAs that are abundant in whole neurons (Fig. 2h). Notably, the second-most increased mRNA term in the KEGG analysis was lysosome (Fig. 3d), perhaps reflecting a compensatory mechanism to generate lysosome-related vesicles when their transport is impaired. Thus, BORCS5 KO decreases axon-enriched mRNAs while increasing neuron-enriched mRNAs in the axon.

The comparison of BORCS5-KO versus WT neurons showed two orders of magnitude fewer genes detected as differentially expressed relative to BORCS5-KO versus WT axons (Supplementary Table 1). Furthermore, KEGG and GO analyses showed little difference in the mRNA profiles of BORCS5 KO versus WT neurons (Extended Data Fig. 4c,d). These observations indicated that the impact of BORCS5 KO was most pronounced in the mRNA profile of axons.

Using RNAscope in situ hybridization (ISH), we observed a reduction in the signal for *RPL41* mRNA in the axon of BORCS5-KO i3Neurons and restoration to normal levels upon re-expression of BORCS5 (Extended Data Fig. 2c,d), confirming the results from RNA-seq (Supplementary Tables 1 and 2). Substitution of alanine for glycine-2, which prevents myristoylation of BORCS5 and its recruitment to lysosomes[31], greatly reduced the ability of BORCS5 to rescue the localization of both lysosome-related vesicles and *RPL41* mRNA (Extended Data Fig. 2a–d).

BORC-KO decreases axonal transport of mRNAs for ribosomal proteins

To directly observe if the depletion of specific mRNAs from the axon of BORCS5-KO neurons was due to decreased transport, we examined the axonal transport of *RPS7* and *RPS27A*, both of which were significantly reduced in BORCS5-KO relative to WT i3Neurons (Supplementary Tables 1 and 2). This analysis was done by stable co-expression of constructs encoding 24 *PP7* RNA stem-loop repeats fused to the mRNA of interest and the PP7 coat protein fused to a triple HaloTag (Fig. 4a)[45]. To visualize the movement of mRNA and lysosome-related vesicles, we plated the co-transfected WT i3Neurons on coverslips and infected them with a lentivirus encoding LAMP1-mNeonGreen. We then incubated the cells overnight with 200 pM of the Halo substrate JF646. As a control, we showed that untransfected WT i3Neurons displayed no Halo signal (Extended Data Fig. 5). Live-cell imaging showed co-movement of LAMP1-mNeonGreen with both *RPS7* and *RPS27A* in WT axons (Fig. 4b–e and Supplementary Videos 1 and 2) and no movement of any of these molecules in BORCS5-KO or BORCS7-KO axons (Fig. 4b–e and Supplementary Data 4).

To determine transport direction, we turned to a system in which WT, BORCS5-KO and BORCS7-KO i3Neurons were grown as three-dimensional (3D) spheroids[46], with axons extending outward (Fig. 4f). In WT axons, we observed both anterograde and retrograde trajectories, as well as a few static foci, labeled for *RPS7* and *RPS27A* (Fig. 4g,h and Supplementary Data 4). In BORCS5-KO and BORCS7-KO axons, we could not detect any moving *RPS7* and *RPS27A* (Fig. 4g,h and Supplementary Data 4). These experiments demonstrated that BORCS5 and BORCS7, and, therefore, transport of lysosome-related vesicles, are required for *RPS7* and *RPS27A* transport within the axon. The absence of retrogradely moving mRNAs is likely secondary to the inhibition of anterograde mRNA transport in the BORCS5-KO and BORCS7-KO neurons.

To confirm that the reduction of *RPS7* and *RPS27A* mRNAs in the axon of BORCS5-KO i3Neurons was due to the inability of lysosome-related vesicles to access the axon, we examined the effect of driving movement of lysosome-related vesicles in these neurons by expressing LAMP1 fused with three copies of a kinesin-binding sequence (KBS) from PLEKHM2 (LAMP1–3×KBS). This manipulation enabled direct coupling of lysosomes to kinesin-1 in the absence of BORC[31,47]. We observed that expression of LAMP1–3×KBS restored the presence of both *RPS7* and *RPS27A* mRNAs within the axon of BORCS5-KO i3Neurons, most noticeably in the central domain of axonal growth cones (Extended Data Figs. 6a,b and 7a,b).

BORC-KO decreases translation of mRNAs in the axon

To examine the impact of the depletion of mRNAs on the synthesis of ribosomal and mitochondrial proteins in BORC-KO axons, we performed puromycin labeling coupled with a proximity ligation assay (puro-PLA) (Fig. 5a)[48]. These experiments revealed translation of mRNAs encoding the ribosomal subunits RPS27A and RPL24, and the mitochondrial proteins COXIV and TOMM20, as puncta in the axons of WT i3Neurons (Fig. 5b). Because the mRNAs encoding these proteins were reduced in BORCS5-KO axons relative to WT axons (Supplementary Tables 1 and 2), we expected a reduction of their synthesis in BORC-KO axons. Indeed, we observed that the number of puro-PLA puncta for all four proteins was reduced in the axons of BORCS5-KO and BORCS7-KO i3Neurons and recovered upon re-expression of the corresponding BORC subunits (Fig. 5b,c). These results demonstrated a reduction in the axonal synthesis of ribosomal and mitochondrial proteins whose mRNAs were decreased upon BORC KO.

Altered properties of axonal mitochondria in BORC-KO i3Neurons

Next, we examined the impact of decreased mRNA levels on the levels of ribosomal and mitochondrial proteins in the axon. We were unable to detect ribosomal proteins by immunoblot analysis of axonal fractions. However, we could readily detect various mitochondrial proteins in the same fractions. We observed that the levels of the mitochondrial complex I–V proteins NDUFS1, SDHA, CYCS, COXIV and ATP5A were significantly reduced in axons from BORCS5-KO and BORCS7-KO i3Neurons, with only two exceptions in which the reductions did not reach statistical significance (NDUFS1 and CYCS in BORCS7-KO cells) (Fig. 6a,b). Axons from BORCS5-KO i3Neurons also exhibited reduced levels of the MIC60 and MIC10 components of the mitochondrial contact site and cristae organizing system (MICOS) in the inner mitochondrial membrane (Fig. 6a,b). In axons from BORCS7-KO i3Neurons, the reductions in MICOS proteins did not reach statistical significance (Fig. 6a,b). Thus, there was an overall trend toward lower levels of mitochondrial proteins in the BORC-KO axons, although these reductions were less dramatic than those of the corresponding mRNAs (Supplementary Tables 1 and 2).

Fig. 3 | Depletion of mRNAs encoding ribosomal and mitochondrial proteins from the axon of BORCS5-KO i3Neurons. a, MA plot for protein-coding genes in BORCS5-KO axons versus WT axons identified by RNA-seq. Each dot represents a protein-coding gene with its mean normalized read count (*x* axis) and $\log_2$ fold change (*y* axis). Insignificant (FDR > 0.1), significant (FDR < 0.1) and top 20 (lowest FDR) protein-coding DEGs for both up or down DEGs are colored gray, black and red, respectively. Top 20 up or down genes are indicated. **b**, Expression profiling of selected axonal genes shown to be axon enriched in i3Neurons (the present study) and other neuronal types[38,40–42]. Each dot represents a biological replicate, with $\log_{10}$-normalized read counts for each gene on the *y* axis. **c**,**d**, Dot plots for gene sets in GO Cellular Component (**c**) and KEGG pathways (**d**). Left panel (down) represents the set of genes that had a negative interaction term in the axon and no change in neurons due to BORCS5 KO; right panel (up) shows the set of genes that had a positive interaction term in the axon and no change in neurons due to BORCS5 KO. Enriched gene sets in **c** and **d** were arranged by statistical significance (FDR). The z-score captures both the direction of changes and the number of genes changing in each direction. A larger absolute z-score indicates a more biased direction toward up or down. Statistical significance was calculated by one-sided Fisher's exact test. *P* values were adjusted for multiple comparisons using the Benjamini–Hochberg method. **e**, Enrichment map for top 12 KEGG gene sets decreased in BORCS5-KO axons versus WT axons in RNA-seq. The gene sets in the left panel of **d** were clustered by a community detection algorithm. The map consists of nodes for pathways and edges indicating the presence of DEGs that are concurrently found between the pathways.

https://doi.org/10.1038/s41593-024-01619-1

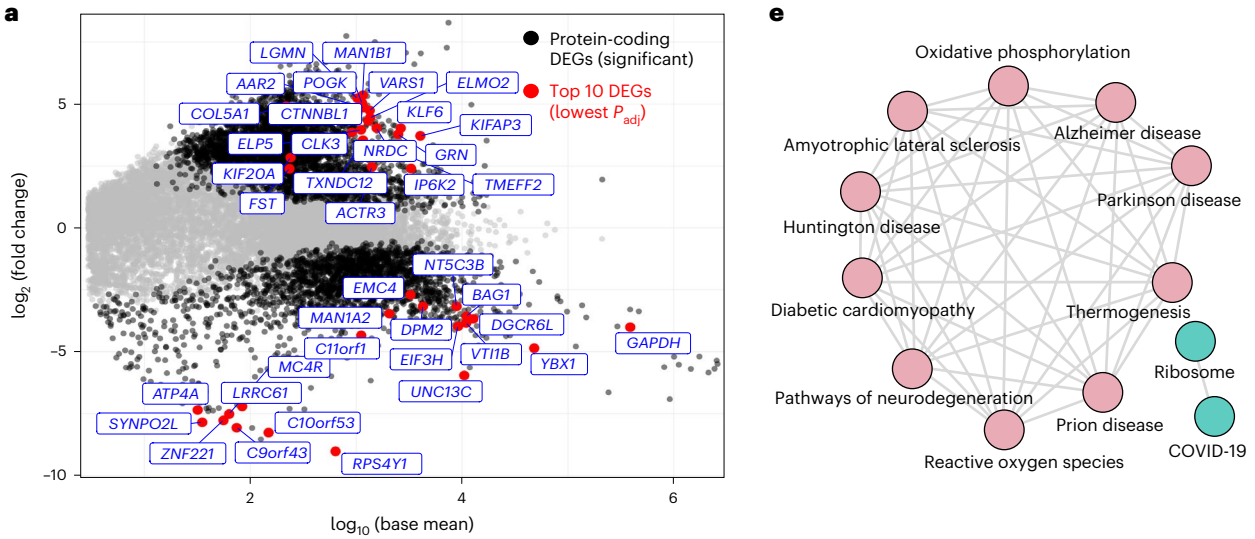

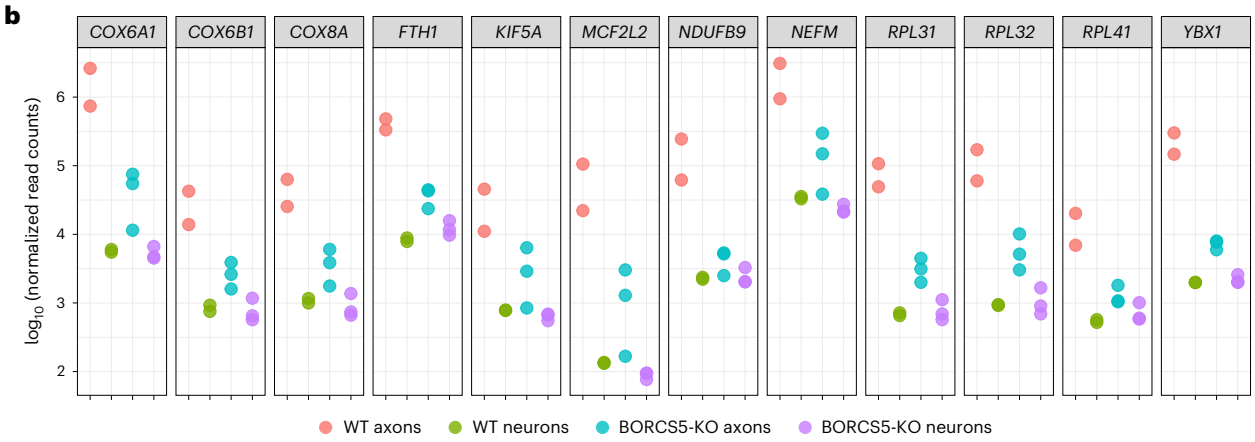

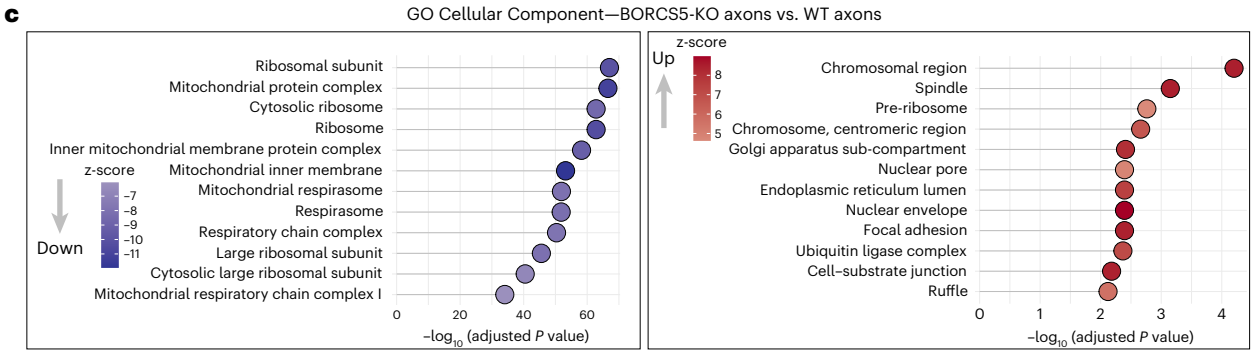

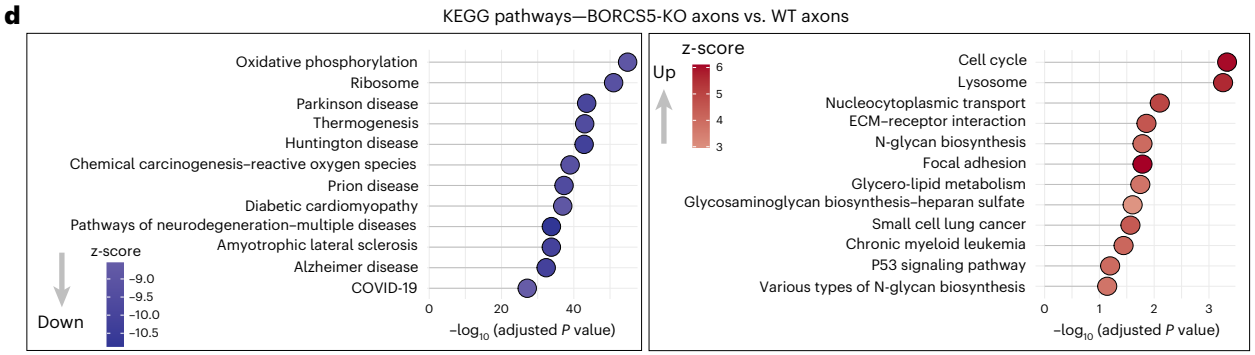

https://doi.org/10.1038/s41593-024-01619-1

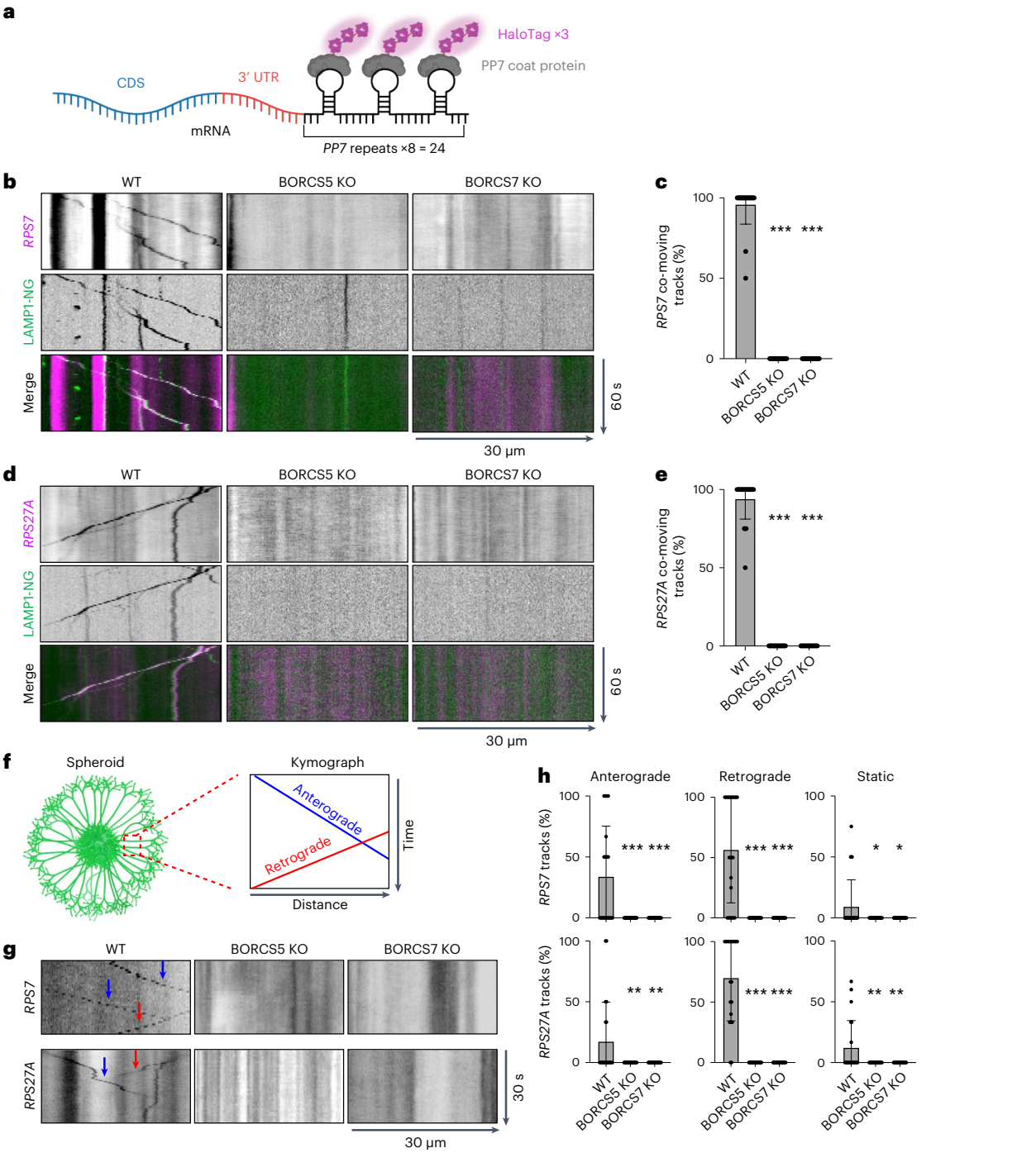

Fig. 4 | Transport of mRNAs encoding ribosomal proteins is reduced in the axon of BORC-subunit-KO i3Neurons. a, Constructs used for RNA visualization. A construct encoding HaloTags fused to the PP7 coat protein was stably co-expressed with the coding sequencing (CDS) of the gene of interest followed by its 3′ UTR, fused to PP7 RNA stem-loop repeats in WT, BORCS5-KO or BORCS7-KO i3Neurons. **b**,**d**, Kymographs of *RPS7* (**b**) or *RPS27A* (**d**) i3Neurons co-expressing the constructs described in **a** were transduced with LAMP1-mNeonGreen (LAMP1-NG) and incubated with the fluorescent Halo substrate JF646 to image axonal lysosome-related vesicle and mRNA movement, respectively. Axons were imaged live for 60 s. Kymographs were generated from Supplementary Videos 1 and 2. Single-color images are represented in inverted grayscale. See Extended Data Fig. 6 for negative control of JF646 staining. **c**,**e**, Quantification of co-moving LAMP1-NG and *RPS7* (**c**) or *RPS27A* (**e**) mRNA tracks. Values are the mean ± s.d. of ~22 kymographs from ~22 neurons per condition and are expressed as the percentage of the indicated marker that co-moves with LAMP1-NG. Statistical significance was calculated by one-way ANOVA with Dunnett's multiple comparisons test. BORCS5 KO versus WT ***$P < 0.001$ and BORCS7 KO versus WT ***$P < 0.001$ for both **c** and **e**. **f**, Scheme of a neuronal spheroid. Axons were imaged live for 30 s, and kymographs were generated from the videos. Lines with negative or positive slopes represent anterograde or retrograde movement, respectively. **g**, Kymographs of axonal mRNA movement in i3Neurons co-expressing combinations of *RPS7*-PP7 or *RPS27A*-PP7 repeats and HaloTag-PP7 coat constructs were generated from spheroids. **h**, Quantification of anterograde, retrograde and static *RPS7* or *RPS27A* mRNA tracks. Values are the mean ± s.d. from ~20 kymographs from ~20 neurons per condition and are expressed as the percentage of the indicated marker in anterograde, retrograde or static particles. Statistical significance was calculated by one-way ANOVA with Dunnett's multiple comparisons test. *P* values relative to WT: *RPS7* anterograde, BORCS5 KO ***$P < 0.001$, BORCS7 KO ***$P < 0.001$; retrograde, BORCS5 KO ***$P < 0.001$, BORCS7 KO ***$P < 0.001$; static, BORCS5 KO *$P = 0.023$, BORCS7 KO *$P = 0.023$. *RPS27A* anterograde, BORCS5 KO **$P = 0.004$, BORCS7 KO **$P = 0.004$; retrograde, BORCS5 KO ***$P < 0.001$, BORCS7 KO ***$P < 0.001$; static, BORCS5 KO **$P = 0.003$, BORCS7 KO **$P = 0.003$.

https://doi.org/10.1038/s41593-024-01619-1

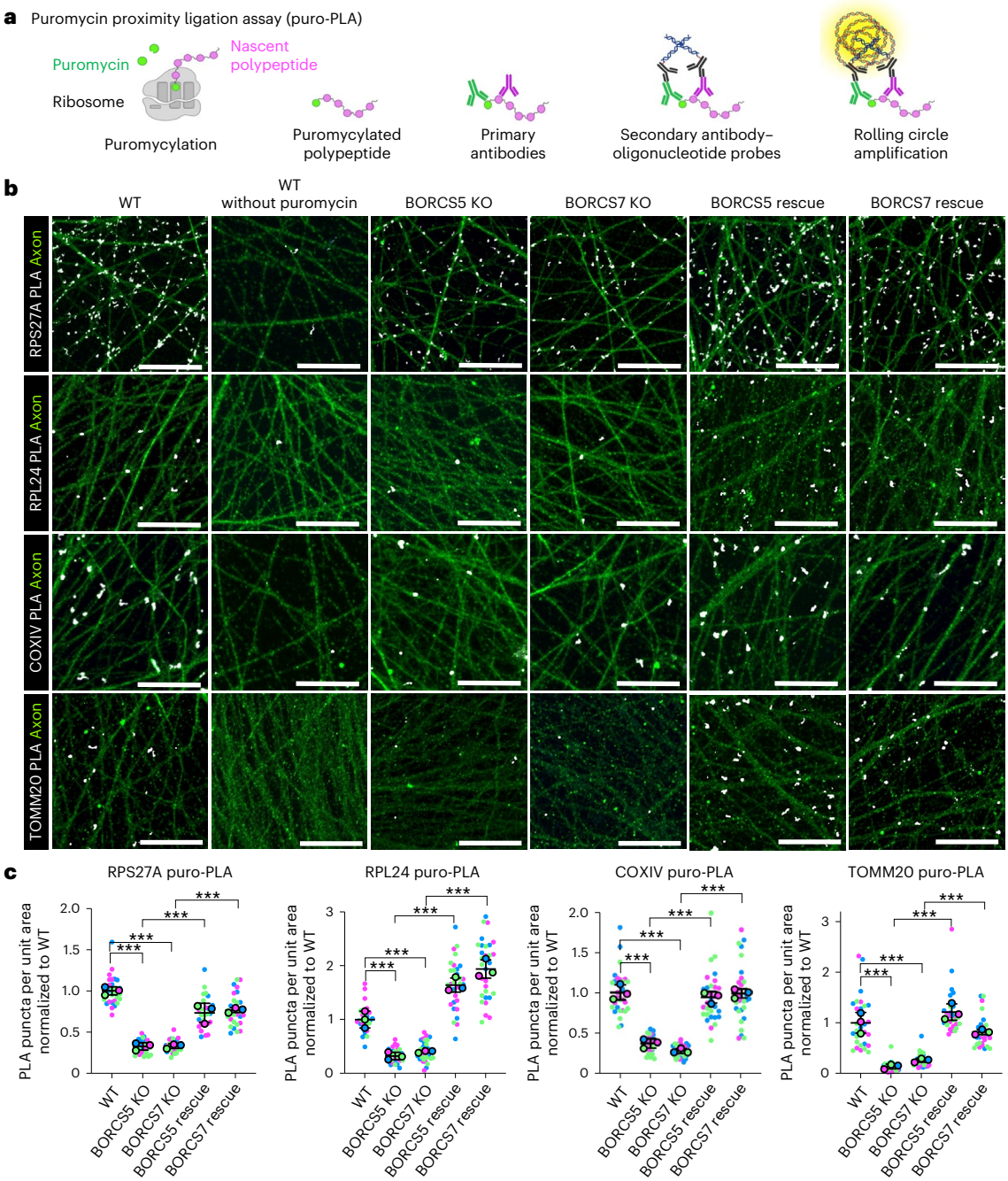

Fig. 5 | Decreased translation of mRNAs encoding ribosomal and mitochondrial proteins in axons from BORC-KO neurons. a, Schematic representation of puro-PLA (see Methods for description)[48]. **b**, WT, BORCS5-KO, BORCS7-KO, BORCS5-KO rescue and BORCS7-KO rescue i3Neurons grown for 25 d on glass coverslips were double stained with puro-PLA for the ribosomal proteins RPS27A or RPL24, or the mitochondrial proteins COXIV or TOMM20 (all in grayscale), and MAP2 for faint axonal staining as described above (green channel). The axonal field was imaged by confocal fluorescence microscopy. Scale bars, 20 µm. The experiment was repeated three times. **c**, Quantification of the number of puro-PLA puncta per unit axon area from three independent experiments such as that shown in **b**. Results are represented as SuperPlots[77] showing the individual data points in different colors, the mean from each experiment and the mean of the means ± s.d. Statistical significance was calculated by one-way ANOVA with Tukey's multiple comparisons test. RPS27A: BORCS5 KO versus WT ***$P < 0.001$, BORCS7 KO versus WT ***$P < 0.001$, BORCS5 rescue versus BORCS5 KO ***$P < 0.001$, BORCS7 rescue versus BORCS7 KO ***$P < 0.001$. RPL24: BORCS5 KO versus WT ***$P < 0.001$, BORCS7 KO versus WT ***$P < 0.001$, BORCS5 rescue versus BORCS5 KO ***$P < 0.001$, BORCS7 rescue versus BORCS7 KO ***$P < 0.001$. COXIV: BORCS5 KO versus WT ***$P < 0.001$, BORCS7 KO versus WT ***$P < 0.001$, BORCS5 rescue versus BORCS5 KO ***$P < 0.001$, BORCS7 rescue versus BORCS7 KO ***$P < 0.001$. TOMM20: BORCS5 KO versus WT ***$P < 0.001$, BORCS7 KO versus WT ***$P < 0.001$, BORCS5 rescue versus BORCS5 KO ***$P < 0.001$, BORCS7 rescue versus BORCS7 KO ***$P < 0.001$.

Because complexes I, III and IV of the OXPHOS system are proton pumps that generate the mitochondrial membrane potential (ΔΨm), we hypothesized that the lower levels of components of these complexes could decrease ΔΨm in axons from BORC-KO i3Neurons. Indeed, we observed that, although mitochondria were still present in axons from BORCS-KO i3Neurons (Fig. 1d), they displayed significantly reduced staining for the ΔΨm reporter tetramethylrhodamine ethyl ester (TMRE) (Fig. 6c,d). Because some studies showed a positive correlation

https://doi.org/10.1038/s41593-024-01619-1

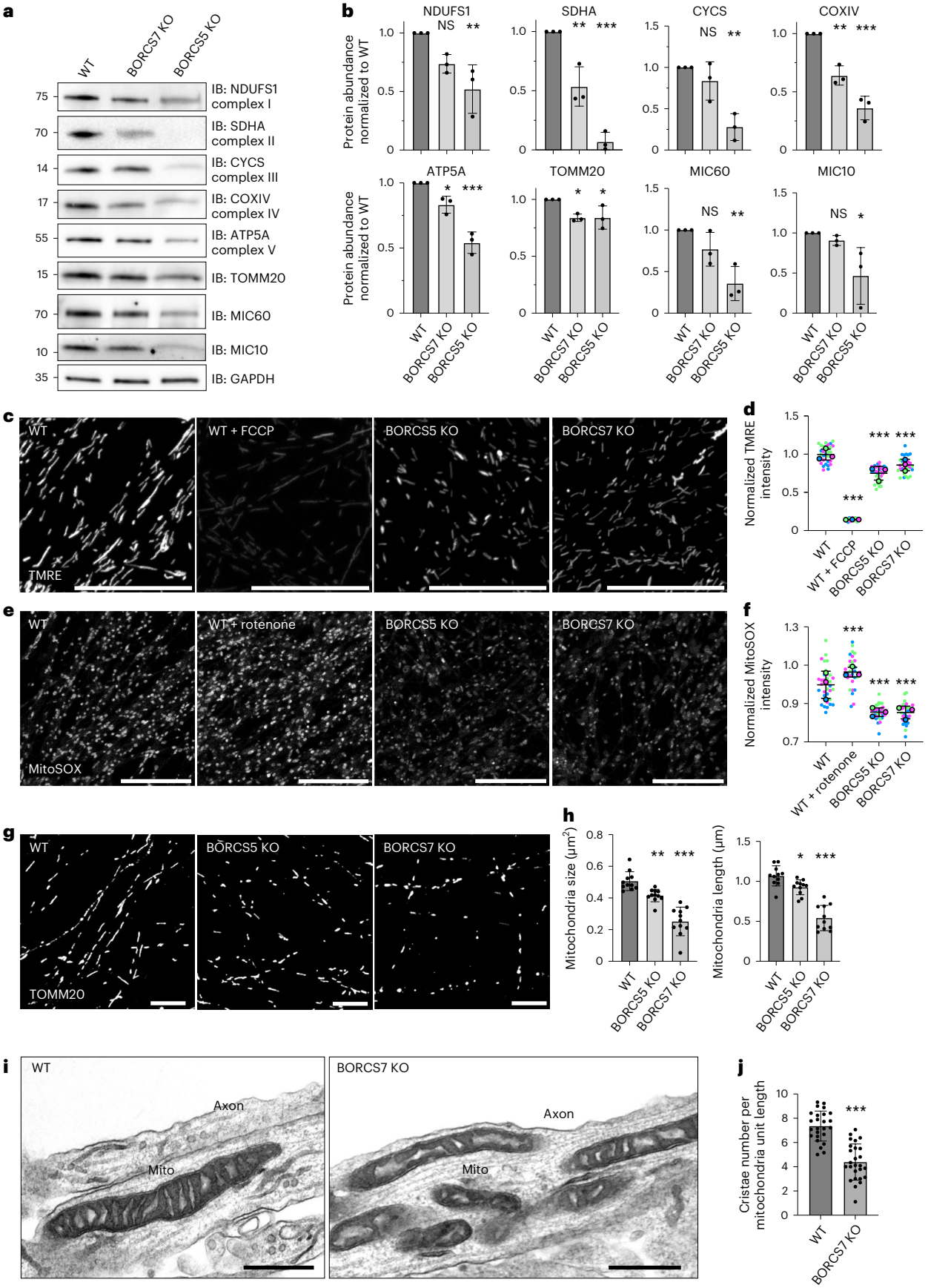

Fig. 6 | Mitochondrial defects in axons from BORC-KO i3Neurons. a, IB analysis of axons from WT, BORCS5-KO or BORCS7-KO i3Neurons cultured in microfluidic devices and analyzed for endogenous mitochondrial proteins and GAPDH (loading control). Molecular mass markers (in kDa) are indicated on the left. **b**, Quantification from three independent experiments such as that shown in **a**. Statistical significance was calculated by one-way ANOVA with Dunnett's multiple comparisons test. Data are represented as mean ± s.d. *P* values relative to WT: NDUFS1, BORCS7 KO $P = 0.078$, BORCS5 KO $^{**}P = 0.006$. SDHA, BORCS7 KO $^{**}P = 0.003$, BORCS5 KO $^{***}P < 0.001$. CYCS, BORCS7 KO $P = 0.417$, BORCS5 KO $^{**}P = 0.003$. COXIV, BORCS7 KO $^{**}P = 0.002$, BORCS5 KO $^{***}P < 0.001$. ATP5A, BORCS7 KO $^{*}P = 0.026$, BORCS5 KO $^{***}P < 0.001$. TOMM20, BORCS7 KO $^{*}P = 0.031$, BORCS5 KO $^{*}P = 0.033$. MIC60, BORCS7 KO $P = 0.231$, BORCS5 KO $^{**}P = 0.005$. MIC10, BORCS7 KO $P = 0.811$, BORCS5 KO $^{*}P = 0.034$. **c**, WT i3Neurons were incubated with the mitochondrial ΔΨm-reporter TMRE with or without FCCP (control), and the axonal field was imaged live. Scale bars, 20 µm. **d**, Quantification of TMRE intensity per unit axonal area from $n = 3$ independent experiments such as that shown in **c**. Data are represented as SuperPlots[77] showing the individual data points, the mean from each experiment and the mean of the means ± s.d. Statistical significance was calculated by one-way ANOVA with Dunnett's multiple comparisons test. *P* values relative to WT: TMRE, WT + FCCP $^{***}P < 0.001$, BORCS5 KO $^{***}P < 0.001$, BORCS7 KO $^{***}P < 0.001$. **e**, i3Neurons were incubated with MitoSOX with or without rotenone (control), and the axonal field was imaged live. Scale bars, 20 µm. **f**, Quantification of MitoSOX intensity per unit area of axonal field as described for **d**. Statistical significance was calculated by one-way ANOVA with Dunnett's multiple comparisons test. *P* values relative to WT: MitoSOX, WT + rotenone $^{***}P < 0.001$, BORCS5 KO $^{***}P < 0.001$, BORCS7 KO $^{***}P < 0.001$. **g**, i3Neurons were immunostained for TOMM20, and the axonal field was imaged. Scale bars, 10 µm. **h**, Size and length of axonal mitochondria measured from experiments such as that shown in **g**. Values are the mean ± s.d. from ~12 fields. Statistical significance was calculated by one-way ANOVA with Dunnett's multiple comparisons test. *P* values relative to WT: Size, BORCS5 KO $^{**}P < 0.006$, BORCS7 KO $^{***}P < 0.001$. Length, BORCS5 KO $^{*}P < 0.025$, BORCS7 KO $^{***}P < 0.001$. **i**, Axonal mitochondria were analyzed by TEM in $n = 2$ independent experiments. Scale bars, 400 nm. **j**, Quantification of the number of cristae per mitochondrial unit length from $n = 26$ axons in $n = 2$ independent experiments. Values are the mean ± s.d. from images like the ones in **i**. Statistical significance was calculated using unpaired two-tailed Student's *t*-test. BORCS7 KO versus WT $^{***}P < 0.001$.

between ΔΨm and production of ROS[49], we also examined ROS levels in the axon of WT and KO i3Neurons by staining with MitoSOX (Fig. 6e,f). We observed that axonal mitochondria from BORCS5-KO and BORCS7-KO i3Neurons also exhibited reduced MitoSOX fluorescence (Fig. 6e,f).

Although mitochondria were present in the axons of BORC-KO i3Neurons, morphological analyses of immunofluorescence microscopy images showed that, on average, they had reduced surface area and length (Fig. 6g,h). In addition, transmission electron microscopy (TEM) of i3Neurons showed that, whereas WT axonal mitochondria displayed a regular spacing of their cristae, BORCS7-KO axonal mitochondria exhibited misaligned and deformed cristae (Fig. 6i). The number of cristae was also reduced in BORCS7-KO i3Neurons (Fig. 6j).

Taken together, these experiments demonstrated that axonal mitochondria are defective in BORC-KO i3Neurons, a phenotype that is likely secondary to the depletion of lysosome-related vesicles transporting mRNAs for synthesis of mitochondrial proteins.

Accumulation of autophagosomes and swellings in BORC-KO axons

Loss of mitochondrial ΔΨm is known to trigger mitophagy[50]. Immunofluorescence microscopy analyses indeed showed that BORCS5 or BORCS7 KO caused a marked increase in axonal puncta stained for the autophagosome marker LC3B[51] (Fig. 7a,b), as previously observed in other models of axonal dystrophy and degeneration[52–54]. The LC3B increase was reversed by re-expression of BORCS5 or BORCS7 in the corresponding BORC-KO i3Neurons (Fig. 7a,b). In BORC-KO i3Neurons, the LC3B puncta were often found in association with mitochondria stained for CYCS (Fig. 7a, yellow arrows). LC3B accumulation was most striking in axonal swellings, which were numerous in BORC-KO i3Neurons (Fig. 7c,d and Extended Data Fig. 8a). The swellings contained many small mitochondria (Fig. 7d), which, in some cases, were engulfed within LC3B-positive autophagosomes (Fig. 7e, arrow). TEM also showed accumulation of autophagosomes and mitochondria in axonal swellings of BORC-KO i3Neurons, with some mitochondria found within the autophagosomes (Fig. 7f, arrow). In addition, the axonal swellings were heavily stained for Tau (Fig. 7g) and exhibited an aberrant swirl-like organization of microtubules (Fig. 7h and Extended Data Fig. 8b), both characteristic of axonal degeneration[55,56].

We corroborated some of these findings in day-in-vitro (DIV) 7 cortical neurons from homozygous BORCS5-KO mouse embryonic day (E) 17 embryos[11]. We observed that, like the BORCS5-KO human axons, BORCS5-KO mouse axons displayed swellings (Fig. 8a) containing Tau, mitochondria, LC3B (Fig. 8b–e) and microtubule swirls (Fig. 8f,g). Although axon fragmentation was not apparent in BORCS5-KO i3Neurons for up to 45 d in culture, it was clearly seen in BORCS5-KO mouse neurons cultured for 10 d (Fig. 8h,i). This difference could indicate that native mouse neurons are more vulnerable or represent a different developmental stage than in vitro differentiated i3Neurons.

Finally, immunohistochemical analysis of the sciatic nerve also showed the presence of numerous swellings labeled for the axonal marker NFH, Tau and LC3B but not LAMP1 in BORCS5-KO axons (Extended Data Fig. 9a–c). Furthermore, TEM revealed the presence of autophagosomes, some containing engulfed mitochondria, in axons from the corpus callosum of BORCS5-KO but not WT mouse E17 embryos (Extended Data Fig. 10a,b).

We conclude that BORC KO in both human and mouse neurons causes accumulation of axonal autophagosomes in association with mitochondria, suggestive of increased mitophagy. This accumulation is particularly striking in axonal swellings containing Tau and

Fig. 7 | Accumulation of axonal autophagosomes and swellings in BORC-KO i3Neurons. a, i3Neurons were immunostained for LC3B (autophagosomes) and CYCS (mitochondria), and the axonal fields were imaged. Single-channel images are shown in grayscale. Arrows in the merge panels indicate LC3B puncta in association with mitochondria. Scale bars, 10 µm. **b**, Quantification of the number of LC3B puncta per unit of axonal area from three independent experiments, such as those shown in **a**. Data are represented as SuperPlots[77] showing the individual data points, the mean from each experiment and the mean of the means ± s.d. Statistical significance was calculated by one-way ANOVA with Dunnett's multiple comparisons test. Significance relative to WT: BORCS5 KO $^{***}P < 0.001$, BORCS7 KO $^{***}P < 0.001$, BORCS5 KO rescue $P < 0.981$, BORCS7 KO rescue $P < 0.468$. **c**, BORCS7-KO i3Neurons were quadruple stained for LC3B, CYCS, MAP2 and nuclear DNA (DAPI). The top image shows axonal swellings in *x*–*y* view. Scale bar, 10 µm. The bottom image shows a *z* axis view of the dashed rectangle. **d**, 3D volume rendering using Imaris of a swelling from a BORCS7-KO i3Neuron immunostained for LC3B and CYCS as above. Scale bars, 5 µm. **e**, Zoomed-in view of the boxed area in the 3D rendering from **d** shows a mitochondrion inside an autophagosome (white arrow). Scale bar, 1 µm. **f**, TEM of axons showing swellings filled with autophagosomes (AP) and mitochondria (Mito). Arrow indicates a mitochondrion inside an autophagosome. Scale bars, 200 nm. **g**, Swelling from a BORCS7-KO i3Neuron immunostained for TOMM20 and the microtubule-associated protein Tau. Scale bars, 5 µm. See also Extended Data Fig. 8a. **h**, i3Neurons sequentially stained with SPY650-tubulin and MitoTracker Green (mitochondria) were imaged live on an Airyscan confocal microscope. Arrow points at microtubule swirls in an axonal swelling. Scale bars, 10 µm. See also Extended Data Fig. 8b. All neurons shown in **c**–**h** were grown for 25 d, and the experiments were repeated three times.

https://doi.org/10.1038/s41593-024-01619-1

microtubule swirls, all conditions that are likely associated with axonal dysfunction and degeneration.

Discussion

Our study demonstrates that preventing transport of lysosome-related vesicles into the axon by BORC KO causes depletion of a large subset of mRNAs from the axon but not the whole neuron. This subset comprises many nuclear-encoded mRNAs encoding ribosomal and mitochondrial proteins, likely as a result of reduced RNA granule association with and hitchhiking on lysosomal vesicles[19,23]. Depletion of these mRNAs is linked to decreased synthesis of ribosomal and mitochondrial proteins as well as alterations in mitochondrial morphology, ΔΨm, ROS and autophagy in the axon. These defects likely underlie the development of axonal swellings as a prelude to axonal degeneration and fragmentation. This series of events probably explains the neurodevelopmental/neurodegenerative phenotype of mice with homozygous mutations[7,11,57]

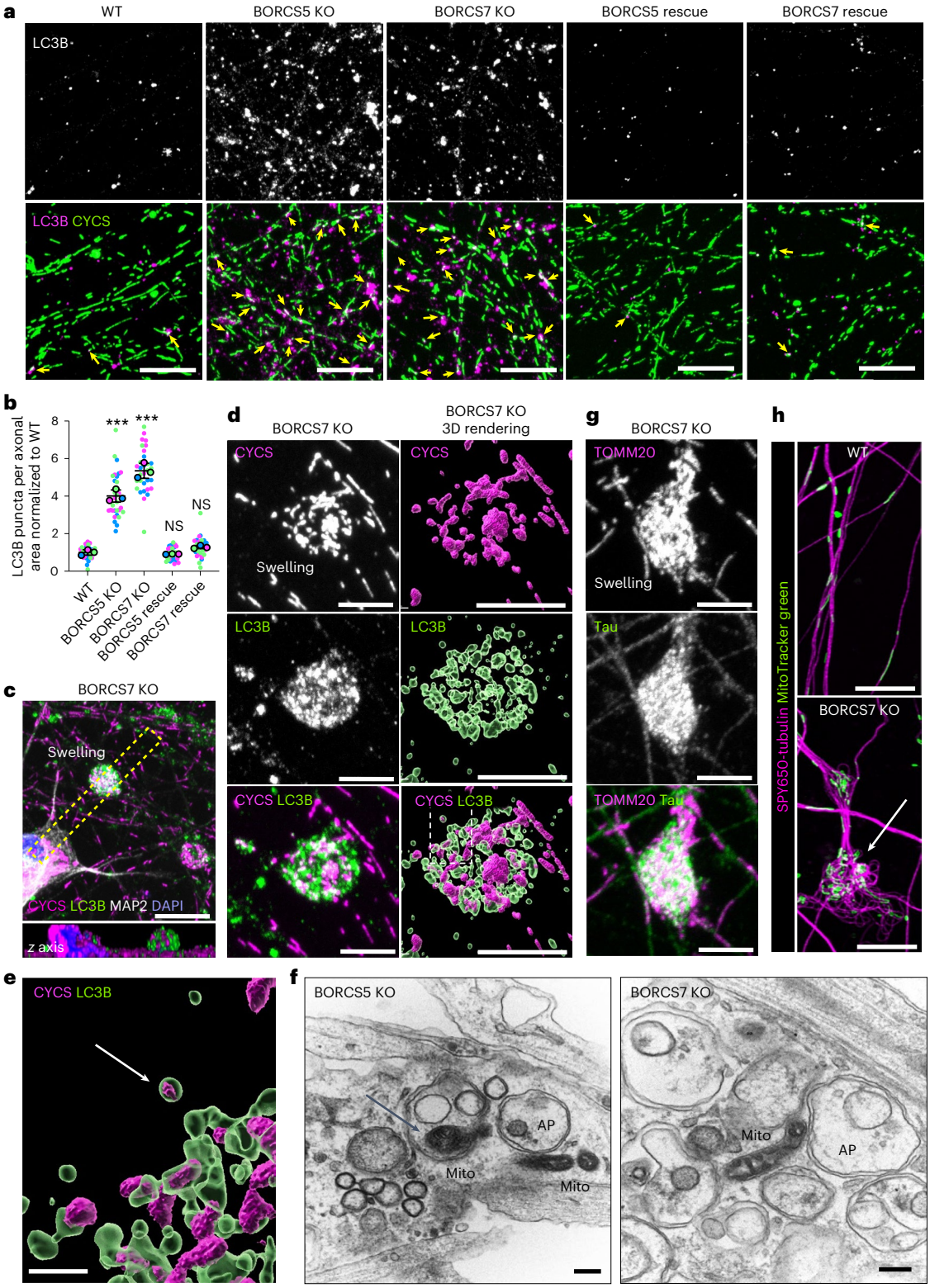

https://doi.org/10.1038/s41593-024-01619-1

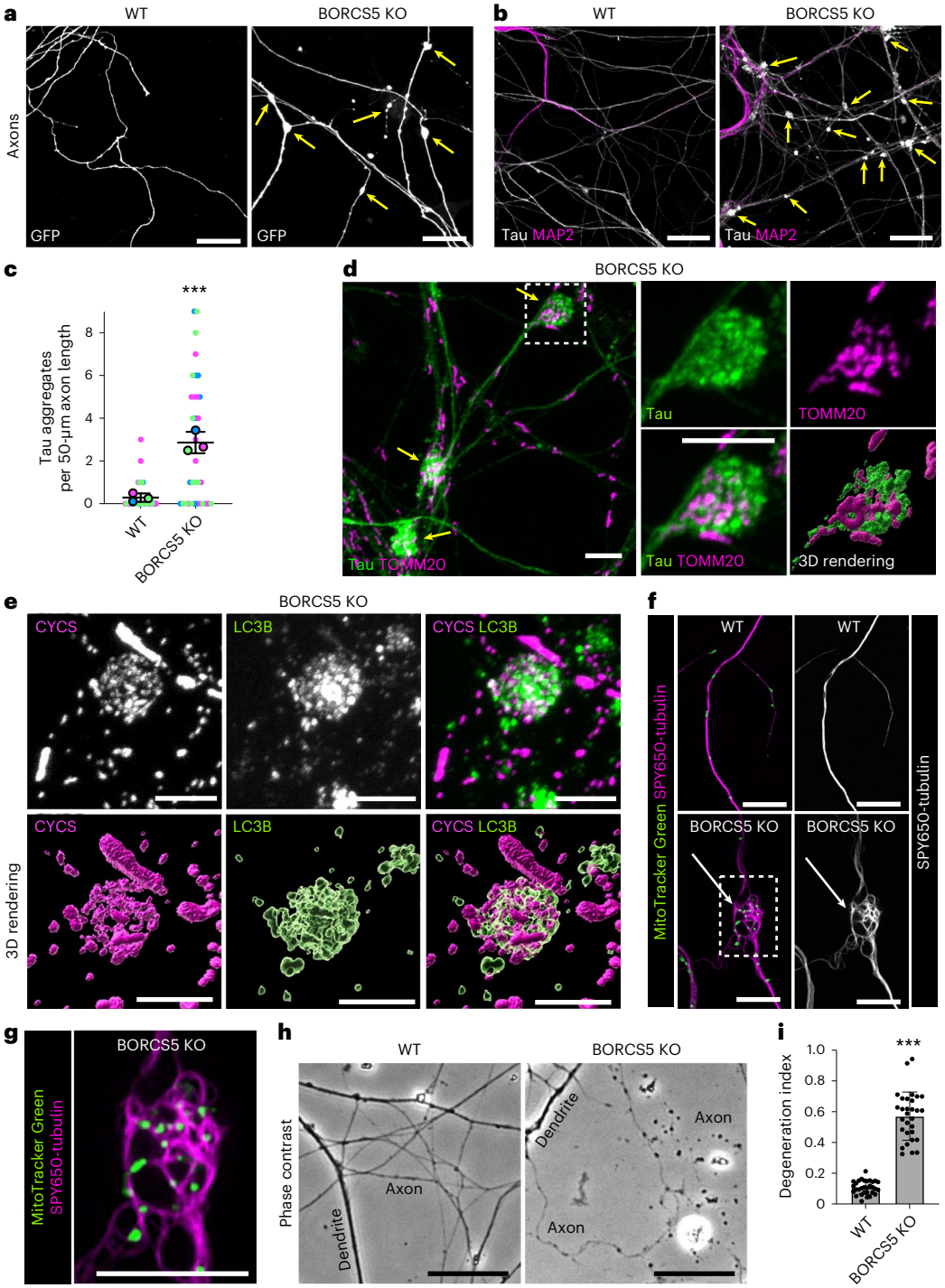

Fig. 8 | Accumulation of axonal autophagosomes and swellings in cortical neurons from BORCS5-KO mice. a, Cortical neurons isolated from WT and BORCS5-KO E17 mouse embryos[11] were transfected with a plasmid expressing soluble GFP. Arrows indicate axonal swellings. Scale bars, 20 µm. The experiment was repeated three times. **b**, Cortical neurons from WT and BORCS5-KO mice were immunostained for Tau (axon) and MAP2 (soma and dendrites). Arrows indicate the accumulation of Tau-positive aggregates in the swellings. Scale bars, 20 µm. **c**, Quantification of the number of Tau-positive swellings per unit length of axon from three experiments, such as shown in **b**. Data are represented as SuperPlots[77] showing the individual data points, the mean from each experiment and the mean of the means ± s.d. Statistical significance was calculated using an unpaired two-tailed Student's *t*-test. BORCS5 KO versus WT ***$P < 0.001$. **d**, Axonal swellings (arrows) in BORCS5-KO mouse cortical neurons immunostained with antibodies to Tau and TOMM20 (mitochondria). The four images on the right are magnified views and a 3D rendering of the boxed area. Scale bars, 5 µm. **e**, Immunofluorescence microscopy and 3D rendering of axonal swellings in cortical neurons from BORCS5-KO mice stained for LC3B (autophagosomes) and CYCS (mitochondria). Scale bars, 5 µm. **f**, Axons from WT and BORCS5-KO mouse cortical neurons sequentially stained with SPY650-tubulin (tubulin) for 1 h and MitoTracker Green (mitochondria) for 10 min were imaged live on an Airyscan confocal microscope. Arrows point to microtubule swirls in an axonal swelling. Scale bars, 10 µm. **g**, Zoomed-in view of the boxed area from **f** shows microtubule swirls in an axonal swelling. Scale bar, 20 µm. All the experiments shown in **d**–**f** were repeated three times. **h**, Phase-contrast microscopy of axons from WT and BORCS5-KO mouse cortical neurons. Notice fragmentation in the BORCS5-KO axons. Scale bars, 5 µm. **i**, Quantification of axon DI from two independent experiments, such as the one shown in **h**. Values are the mean ± s.d. from 30 images. Statistical significance was calculated using an unpaired two-tailed Student's *t*-test. BORCS5 KO versus WT ***$P < 0.001$. Neurons shown in this figure were cultured for 7 d (**a**–**g**) or 10 d (**h** and **i**).

and human patients with biallelic variants[33–35] of BORC-subunit genes. Pathway analysis of the depleted mRNAs also suggests similarities in the pathogenetic mechanisms of BORC deficiency and common neurodegenerative diseases.

BORC is a component of an ensemble that mediates coupling of lysosomes to kinesin-1 and kinesin-3 microtubule motors[6,31,32]. Although the properties of axonal anterograde lysosome-related vesicles differ from those of conventional lysosomes[5,9,12–14], they also depend on BORC for transport into the axon[6,7,9–11,30]. The results presented here and in a previous study[19] show that one function of these vesicles is to carry RNA granules and their mRNA cargo into the axon. Coupling of RNA granules to microtubule motors has also been shown to be mediated directly by interaction of RNPs with the motors[27–29] or indirectly via other organelles, such as mitochondria[24,25], late endosomes/lysosomes[19,23] or early endosomes[23,26]. Each of these mechanisms may account for the axonal transport of different mRNA subsets. The specific depletion of axonal lysosome-related vesicles in BORC-KO i3Neurons allowed us to define the mRNA subset dependent on these vesicles for transport into the axon. This subset is large and comprises mRNAs that are normally abundant in the axon, such as those encoding ribosomal and mitochondrial proteins.

Although most ribosome assembly occurs in the nucleolus, some ribosomal proteins may be added or exchanged immediately after export from the nucleus into the cytoplasm[58–60]. In neurons, some ribosomes are transported into the axon, to some extent also by hitchhiking on lysosomal or late endosomal vesicles[23]. The deployment of ribosomes to the axon enables local synthesis of proteins important for axon maintenance and synaptic function[61–65]. Over time, ribosomal proteins may become damaged[66]. Rather than targeting the whole ribosome for destruction, local translation in the axon may allow for the replacement of the damaged proteins[58,67,68]. Moreover, new synthesis of ribosomal proteins in the axon may enable remodeling of ribosomes in response to physiological or pathological conditions.

The subset of mRNAs depleted in BORC-KO axons also comprises many mRNAs encoding mitochondrial proteins. These include nuclear-encoded and mitochondria-encoded subunits of all five complexes of the electron transport chain as well as nuclear-encoded MICOS components, the mitochondrial import system and mitophagy. As discussed above for ribosomes, these mRNAs are likely translated locally for repair of mitochondria, which are particularly prone to oxidative damage or proteotoxic stress[62,69]. Probably because of reduced synthesis of the corresponding proteins, axonal mitochondria are smaller, have reduced ΔΨm, lower ROS and disorganized cristae and exhibit increased association with autophagosomes. These are all characteristics of dysfunctional mitochondria that are targeted for degradation by mitophagy[70]. However, mitophagy is likely arrested at the stage of autophagosomes because of the absence of axonal lysosomes to confer degradative activity and/or retrograde motility upon fusion[6,10,15]. The accumulation of abnormal mitochondria and autophagosomes is most dramatic in axonal swellings, which may correspond to the eosinophilic spheroids previously observed in nerves from BORCS5-KO mouse embryos[11]. The swellings in BORC-KO human i3Neurons, mouse cortical neurons and sciatic nerves also exhibit accumulation of Tau and microtubule swirls characteristic of other neurodegenerative conditions[55,56]. Indeed, axons from BORCS5-KO mouse cortical neurons undergo fragmentation after 10 d in culture, representing the final stage of a degenerative cascade likely caused by the depletion of axonal lysosome-related vesicles.

In addition to mRNAs encoding ribosomal and mitochondrial proteins, BORC-KO causes depletion of mRNAs encoding cytoskeletal proteins, proteasome subunits, ferritin heavy chain and RBPs from the axon. Moreover, BORC-KO increases the axonal abundance of another subset of mRNAs mainly encoding nuclear, lysosomal, endoplasmic reticulum and cell adhesion proteins. The increased mRNAs could be transported into the axon by coupling of RNA granules to microtubule motors or other organelles. Moreover, BORC normally promotes the recruitment of other ARL8 effectors, including the dynein–dynactin adaptor protein RUFY3 (refs. 71,72) and the endolysosomal tethering complex HOPS[73], to lysosomes. Alterations in all these processes, along with the loss of other lysosomal functions such as degradation or signaling, could additionally contribute to mitochondrial dysfunction and axon degeneration in BORC-KO neurons.

Biallelic variants in BORC subunits have been shown to cause neurodevelopmental or early-infantile neurodegenerative disorders[33–35]. Our results suggest that CNS defects in BORC-variant patients may involve a pathogenetic mechanism like that described in this study. KEGG analysis further suggests a connection between the pathogenetic mechanism of BORC deficiency and those of adult neurodegenerative disorders. What these diseases have in common is the presence of mitochondrial abnormalities, specifically related to OXPHOS, mitophagy and fusion–fission[74–76]. BORC deficiency may, thus, trigger common neurodegenerative pathways at an early age.

In summary, our findings demonstrate that axonal anterograde lysosome-related vesicles carry a large subset of mRNAs, predominantly encoding ribosomal and mitochondrial proteins. It is likely that local translation of these mRNAs enables the replacement of damaged ribosomal and mitochondrial proteins, ultimately contributing to the maintenance of ribosomal and mitochondrial homeostasis in the axon.

Online content

Any methods, additional references, Nature Portfolio reporting summaries, source data, extended data, supplementary information, acknowledgements, peer review information; details of author contributions and competing interests; and statements of data and code availability are available at https://doi.org/10.1038/s41593-024-01619-1.

References

1. Ballabio, A. & Bonifacino, J. S. Lysosomes as dynamic regulators of cell and organismal homeostasis. *Nat. Rev. Mol. Cell Biol.* **21**, 101–118 (2020).
2. Shin, H. R. & Zoncu, R. The lysosome at the intersection of cellular growth and destruction. *Dev. Cell* **54**, 226–238 (2020).
3. Ferguson, S. M. Neuronal lysosomes. *Neurosci. Lett.* **697**, 1–9 (2019).
4. Roney, J. C., Cheng, X. T. & Sheng, Z. H. Neuronal endolysosomal transport and lysosomal functionality in maintaining axonostasis. *J. Cell Biol.* **221**, e202111077 (2022).
5. Lee, S., Sato, Y. & Nixon, R. A. Lysosomal proteolysis inhibition selectively disrupts axonal transport of degradative organelles and causes an Alzheimer's-like axonal dystrophy. *J. Neurosci.* **31**, 7817–7830 (2011).
6. Farías, G. G., Guardia, C. M., De Pace, R., Britt, D. J. & Bonifacino, J. S. BORC/kinesin-1 ensemble drives polarized transport of lysosomes into the axon. *Proc. Natl Acad. Sci. USA* **114**, E2955–E2964 (2017).
7. Snouwaert, J. N. et al. A mutation in the Borcs7 subunit of the lysosome regulatory BORC complex results in motor deficits and dystrophic axonopathy in mice. *Cell Rep.* **24**, 1254–1265 (2018).
8. Boecker, C. A., Olenick, M. A., Gallagher, E. R., Ward, M. E. & Holzbaur, E. L. F. ToolBox: live imaging of intracellular organelle transport in induced pluripotent stem cell-derived neurons. *Traffic* **21**, 138–155 (2020).
9. Vukoja, A. et al. Presynaptic biogenesis requires axonal transport of lysosome-related vesicles. *Neuron* **99**, 1216–1232 (2018).
10. Farfel-Becker, T. et al. Neuronal soma-derived degradative lysosomes are continuously delivered to distal axons to maintain local degradation capacity. *Cell Rep.* **28**, 51–64 (2019).
11. De Pace, R. et al. Synaptic vesicle precursors and lysosomes are transported by different mechanisms in the axon of mammalian neurons. *Cell Rep.* **31**, 107775 (2020).

12. Gowrishankar, S. et al. Overlapping roles of JIP3 and JIP4 in promoting axonal transport of lysosomes in human iPSC-derived neurons. *Mol. Biol. Cell* **32**, 1094–1103 (2021).
13. Lie, P. P. Y. et al. Post-Golgi carriers, not lysosomes, confer lysosomal properties to pre-degradative organelles in normal and dystrophic axons. *Cell Rep.* **35**, 109034 (2021).
14. Gowrishankar, S., Wu, Y. & Ferguson, S. M. Impaired JIP3-dependent axonal lysosome transport promotes amyloid plaque pathology. *J. Cell Biol.* **216**, 3291–3305 (2017).
15. Maday, S., Wallace, K. E. & Holzbaur, E. L. Autophagosomes initiate distally and mature during transport toward the cell soma in primary neurons. *J. Cell Biol.* **196**, 407–417 (2012).
16. Cheng, X. T., Zhou, B., Lin, M. Y., Cai, Q. & Sheng, Z. H. Axonal autophagosomes recruit dynein for retrograde transport through fusion with late endosomes. *J. Cell Biol.* **209**, 377–386 (2015).
17. Cason, S. E. et al. Sequential dynein effectors regulate axonal autophagosome motility in a maturation-dependent pathway. *J. Cell Biol.* **220**, e202010179 (2021).
18. Lie, P. P. Y. et al. Axonal transport of late endosomes and amphisomes is selectively modulated by local Ca^{2+} efflux and disrupted by PSEN1 loss of function. *Sci. Adv.* **8**, eabj5716 (2022).
19. Liao, Y. C. et al. RNA granules hitchhike on lysosomes for long-distance transport, using annexin A11 as a molecular tether. *Cell* **179**, 147–164 (2019).
20. Fernandopulle, M. S., Lippincott-Schwartz, J. & Ward, M. E. RNA transport and local translation in neurodevelopmental and neurodegenerative disease. *Nat. Neurosci.* **24**, 622–632 (2021).
21. Gershoni-Emek, N. et al. Localization of RNAi machinery to axonal branch points and growth cones is facilitated by mitochondria and is disrupted in ALS. *Front. Mol. Neurosci.* **11**, 311 (2018).
22. Corradi, E. et al. Axonal precursor miRNAs hitchhike on endosomes and locally regulate the development of neural circuits. *EMBO J.* **39**, e102513 (2020).
23. Cioni, J. M. et al. Late endosomes act as mRNA translation platforms and sustain mitochondria in axons. *Cell* **176**, 56–72 (2019).
24. Cohen, B. et al. Co-transport of the nuclear-encoded *Cox7c* mRNA with mitochondria along axons occurs through a coding-region-dependent mechanism. *J. Cell Sci.* **135**, jcs259436 (2022).
25. Harbauer, A. B. et al. Neuronal mitochondria transport *Pink1* mRNA via synaptojanin 2 to support local mitophagy. *Neuron* **110**, 1516–1531 (2022).
26. Schuhmacher, J. S. et al. The Rab5 effector FERRY links early endosomes with mRNA localization. *Mol. Cell* **83**, 1839–1855 (2023).
27. Dictenberg, J. B., Swanger, S. A., Antar, L. N., Singer, R. H. & Bassell, G. J. A direct role for FMRP in activity-dependent dendritic mRNA transport links filopodial-spine morphogenesis to fragile X syndrome. *Dev. Cell* **14**, 926–939 (2008).
28. Fukuda, Y. et al. Binding and transport of SFPQ-RNA granules by KIF5A/KLC1 motors promotes axon survival. *J. Cell Biol.* **220**, e202005051 (2021).
29. Baumann, S. et al. A reconstituted mammalian APC-kinesin complex selectively transports defined packages of axonal mRNAs. *Sci. Adv.* **6**, eaaz1588 (2020).
30. Rosa-Ferreira, C. & Munro, S. Arl8 and SKIP act together to link lysosomes to kinesin-1. *Dev. Cell* **21**, 1171–1178 (2011).
31. Pu, J. et al. BORC, a multisubunit complex that regulates lysosome positioning. *Dev. Cell* **33**, 176–188 (2015).
32. Guardia, C. M., Farías, G. G., Jia, R., Pu, J. & Bonifacino, J. S. BORC functions upstream of kinesins 1 and 3 to coordinate regional movement of lysosomes along different microtubule tracks. *Cell Rep.* **17**, 1950–1961 (2016).
33. Charng, W. L. et al. Exome sequencing in mostly consanguineous Arab families with neurologic disease provides a high potential molecular diagnosis rate. *BMC Med. Genomics* **9**, 42 (2016).
34. Bertoli-Avella, A. M. et al. Combining exome/genome sequencing with data repository analysis reveals novel gene-disease associations for a wide range of genetic disorders. *Genet. Med.* **23**, 1551–1568 (2021).
35. De Pace, R. et al. Biallelic *BORCS8* variants cause an infantile-onset neurodegenerative disorder with altered lysosome dynamics. *Brain* https://doi.org/10.1093/brain/awad427 (2023).
36. Wang, C. et al. Scalable production of iPSC-derived human neurons to identify Tau-lowering compounds by high-content screening. *Stem Cell Reports* **9**, 1221–1233 (2017).
37. Fernandopulle, M. S. et al. Transcription factor–mediated differentiation of human iPSCs into neurons. *Curr. Protoc. Cell Biol.* **79**, e51 (2018).
38. Briese, M. et al. Whole transcriptome profiling reveals the RNA content of motor axons. *Nucleic Acids Res.* **44**, e33 (2016).
39. Bigler, R. L., Kamande, J. W., Dumitru, R., Niedringhaus, M. & Taylor, A. M. Messenger RNAs localized to distal projections of human stem cell derived neurons. *Sci. Rep.* **7**, 611 (2017).
40. Nijssen, J., Aguila, J., Hoogstraaten, R., Kee, N. & Hedlund, E. Axon-seq decodes the motor axon transcriptome and its modulation in response to ALS. *Stem Cell Reports* **11**, 1565–1578 (2018).
41. Farias, J., Holt, C. E., Sotelo, J. R. & Sotelo-Silveira, J. R. Axon microdissection and transcriptome profiling reveals the in vivo RNA content of fully differentiated myelinated motor axons. *RNA* **26**, 595–612 (2020).
42. Rotem, N. et al. ALS along the axons—expression of coding and noncoding RNA differs in axons of ALS models. *Sci. Rep.* **7**, 44500 (2017).
43. Zivraj, K. H. et al. Subcellular profiling reveals distinct and developmentally regulated repertoire of growth cone mRNAs. *J. Neurosci.* **30**, 15464–15478 (2010).
44. Jung, J. et al. mRNA transport, translation, and decay in adult mammalian central nervous system axons. *Neuron* **111**, 650–668 (2022).
45. Wu, B., Chao, J. A. & Singer, R. H. Fluorescence fluctuation spectroscopy enables quantitative imaging of single mRNAs in living cells. *Biophys. J.* **102**, 2936–2944 (2012).
46. Paşca, A. M. et al. Functional cortical neurons and astrocytes from human pluripotent stem cells in 3D culture. *Nat. Methods* **12**, 671–678 (2015).
47. Pernigo, S., Lamprecht, A., Steiner, R. A. & Dodding, M. P. Structural basis for kinesin-1:cargo recognition. *Science* **340**, 356–359 (2013).
48. tom Dieck, S. et al. Direct visualization of newly synthesized target proteins in situ. *Nat. Methods* **12**, 411–414 (2015).
49. Turrens, J. F. Mitochondrial formation of reactive oxygen species. *J. Physiol.* **552**, 335–344 (2003).
50. Narendra, D., Tanaka, A., Suen, D. F. & Youle, R. J. Parkin is recruited selectively to impaired mitochondria and promotes their autophagy. *J. Cell Biol.* **183**, 795–803 (2008).
51. Kabeya, Y. et al. LC3, a mammalian homologue of yeast Apg8p, is localized in autophagosome membranes after processing. *EMBO J.* **19**, 5720–5728 (2000).
52. Wang, Q. J. et al. Induction of autophagy in axonal dystrophy and degeneration. *J. Neurosci.* **26**, 8057–8068 (2006).
53. Cai, Q. et al. Snapin-regulated late endosomal transport is critical for efficient autophagy-lysosomal function in neurons. *Neuron* **68**, 73–86 (2010).
54. Wong, Y. C. & Holzbaur, E. L. The regulation of autophagosome dynamics by huntingtin and HAP1 is disrupted by expression of mutant huntingtin, leading to defective cargo degradation. *J. Neurosci.* **34**, 1293–1305 (2014).
55. Shemesh, O. A., Erez, H., Ginzburg, I. & Spira, M. E. Tau-induced traffic jams reflect organelles accumulation at points of microtubule polar mismatching. *Traffic* **9**, 458–471 (2008).

56. Rafiq, N. M., Lyons, L. L., Gowrishankar, S., De Camilli, P. & Ferguson, S. M. JIP3 links lysosome transport to regulation of multiple components of the axonal cytoskeleton. *Commun. Biol.* **5**, 5 (2022).
57. Zhou, B., Zhu, Y. B., Lin, L., Cai, Q. & Sheng, Z. H. Snapin deficiency is associated with developmental defects of the central nervous system. *Biosci. Rep.* **31**, 151–158 (2011).
58. Lastick, S. M. & McConkey, E. H. Exchange and stability of HeLa ribosomal proteins in vivo. *J. Biol. Chem.* **251**, 2867–2875 (1976).
59. Panse, V. G. & Johnson, A. W. Maturation of eukaryotic ribosomes: acquisition of functionality. *Trends Biochem. Sci.* **35**, 260–266 (2010).
60. Peña, C., Hurt, E. & Panse, V. G. Eukaryotic ribosome assembly, transport and quality control. *Nat. Struct. Mol. Biol.* **24**, 689–699 (2017).
61. Hafner, A. S., Donlin-Asp, P. G., Leitch, B., Herzog, E. & Schuman, E. M. Local protein synthesis is a ubiquitous feature of neuronal pre- and postsynaptic compartments. *Science* **364**, eaau3644 (2019).
62. Hillefors, M., Gioio, A. E., Mameza, M. G. & Kaplan, B. B. Axon viability and mitochondrial function are dependent on local protein synthesis in sympathetic neurons. *Cell Mol. Neurobiol.* **27**, 701–716 (2007).
63. Yoon, B. C. et al. Local translation of extranuclear lamin B promotes axon maintenance. *Cell* **148**, 752–764 (2012).
64. Cosker, K. E., Fenstermacher, S. J., Pazyra-Murphy, M. F., Elliott, H. L. & Segal, R. A. The RNA-binding protein SFPQ orchestrates an RNA regulon to promote axon viability. *Nat. Neurosci.* **19**, 690–696 (2016).
65. Bernabò, P. et al. In vivo translatome profiling in spinal muscular atrophy reveals a role for SMN protein in ribosome biology. *Cell Rep.* **21**, 953–965 (2017).
66. Shcherbik, N. & Pestov, D. G. The impact of oxidative stress on ribosomes: from injury to regulation. *Cells* **8**, 1379 (2019).
67. Pulk, A. et al. Ribosome reactivation by replacement of damaged proteins. *Mol. Microbiol.* **75**, 801–814 (2010).
68. Shigeoka, T. et al. On-site ribosome remodeling by locally synthesized ribosomal proteins in axons. *Cell Rep.* **29**, 3605–3619 (2019).
69. Federico, A. et al. Mitochondria, oxidative stress and neurodegeneration. *J. Neurol. Sci.* **322**, 254–262 (2012).
70. Vargas, J. N. S., Hamasaki, M., Kawabata, T., Youle, R. J. & Yoshimori, T. The mechanisms and roles of selective autophagy in mammals. *Nat. Rev. Mol. Cell Biol.* **24**, 167–185 (2022).
71. Keren-Kaplan, T. et al. RUFY3 and RUFY4 are ARL8 effectors that promote coupling of endolysosomes to dynein–dynactin. *Nat. Commun.* **13**, 1506 (2022).
72. Kumar, G. et al. RUFY3 links Arl8b and JIP4-Dynein complex to regulate lysosome size and positioning. *Nat. Commun.* **13**, 1540 (2022).
73. Khatter, D. et al. The small GTPase Arl8b regulates assembly of the mammalian HOPS complex on lysosomes. *J. Cell Sci.* **128**, 1746–1761 (2015).
74. Schapira, A. H. Mitochondrial disease. *Lancet* **368**, 70–82 (2006).
75. Zhu, T., Chen, J. L., Wang, Q., Shao, W. & Qi, B. Modulation of mitochondrial dynamics in neurodegenerative diseases: an insight into prion diseases. *Front. Aging Neurosci.* **10**, 336 (2018).
76. Smith, E. F., Shaw, P. J. & De Vos, K. J. The role of mitochondria in amyotrophic lateral sclerosis. *Neurosci. Lett.* **710**, 132933 (2019).
77. Lord, S. J., Velle, K. B., Mullins, R. D. & Fritz-Laylin, L. K. SuperPlots: communicating reproducibility and variability in cell biology. *J. Cell Biol.* **219**, e202001064 (2020).

Methods

Reagent sources

Sequences of oligonucleotides, company names and catalog numbers for reagents used in this paper are listed in Supplementary Table 3.

Human iPSC culture and neuronal differentiation

Human iPSCs expressing doxycycline-inducible *NGN2* (neurogenin)[36,37] were cultured on Matrigel-coated dishes in Essential 8 Flex Medium (E8Flex) (Thermo Fisher Scientific) according to the manufacturer's instructions. In brief, cells were passaged with Accutase (STEMCELL Technologies) when 70% confluent and seeded into E8Flex supplemented with 10 µM Y-27632 dihydrochloride ROCK inhibitor (S1049, Selleck Chemicals). After 24 h, the medium was replaced with E8Flex without ROCK inhibitor and maintained until the next passage. Differentiation of iPSCs to i3Neurons was performed as described[36,37]. iPSCs were seeded on day 0 in induction medium containing DMEM/F12 (11330032, Gibco, Thermo Fisher Scientific) with 1× non-essential amino acids (NEAAs) (11140050, Gibco, Thermo Fisher Scientific), 1× GlutaMAX (35050061, Gibco, Thermo Fisher Scientific), 1× N2A supplement (17502048, Gibco, Thermo Fisher Scientific), 2 µg ml^{-1} doxycycline (D9891, MilliporeSigma) and 10 µM Y-27632 dihydrochloride ROCK inhibitor (S1049, Selleck Chemicals). The induction medium was changed every day for 3 d. Cells were then lifted with Accutase, counted and plated in neuronal culture medium consisting of BrainPhys medium (5790, STEMCELL Technologies) supplemented with 10 ng ml^{-1} neurotrophin-3 (450-03, PeproTech, Thermo Fisher Scientific), 10 ng ml^{-1} BDNF (450-02, PeproTech, Thermo Fisher Scientific), 1× B-27 supplement serum free (17504044, Gibco, Thermo Fisher Scientific), 2 µg ml^{-1} doxycycline (D9891, MilliporeSigma) and 1 µg ml^{-1} mouse laminin (23017015, Gibco, Thermo Fisher Scientific). The coverslips for growth of i3Neurons were pre-treated with poly-L-lysine hydrobromide (P2636, MilliporeSigma) and laminin (11243217001, Roche, MilliporeSigma). Every 3 d, half of the medium was removed, and an equal volume of fresh medium was added to maintain neuronal health.

Mouse husbandry

All mouse procedures were conducted following the National Institutes of Health Guide for the Care and Use of Laboratory Animals, under protocol 21-021 that received ethical approval by the Eunice Kennedy Shriver National Institute of Child Health and Human Development (NICHD) Animal Care and Use Committee. Mouse husbandry is described in detail in Supplementary Data 1.

Culture of primary cortical neurons

Primary cortical neurons were prepared from mice as previously described[78]. In brief, after timed pregnancies, E17 mice were harvested and euthanized by decapitation. The brain was collected, and meninges were removed, after which cortices were isolated in sterile HBSS (20 mM HEPES, pH 7.5). Cortices were then treated with 0.25% trypsin (Gibco, Thermo Fisher Scientific) and 100 µg ml^{-1} DNase (Roche) for 15 min at 37 °C. To stop trypsin enzymatic action, one volume of DMEM without phenol red (Thermo Fisher Scientific), supplemented with 4.5 g L^{-1} glucose, 25 mM HEPES, 10% heat-inactivated horse serum (Gibco, Thermo Fisher Scientific) and 100 U ml^{-1} penicillin–streptomycin (Quality Biological) (adhesion medium), was added. The tissue was then pipetted through a 10-ml serological pipette to disrupt it mechanically. Single cells were then strained through a 70-µm nylon filter (Corning) and centrifuged at 700*g* for 10 min. The cell pellet was resuspended in 5 ml of adhesion medium, and cells were counted. Cells (80,000) were plated on 18-mm glass coverslips previously coated with polylysine and laminin. After 3 h, the medium was changed to complete Neurobasal medium (CNB) consisting of Neurobasal medium (Gibco, Thermo Fisher Scientific) supplemented with 1× B27 serum free (Thermo Fisher Scientific), 4.5 g L^{-1} glucose (Quality Biological) and 100 U ml^{-1} penicillin–streptomycin (Quality Biological). For timed pregnancies, mice of both sexes of approximately 6 weeks of age were used.

CRISPR–Cas9 KO of *BORCS5* or *BORCS7*

To inactivate the *BORCS5* and *BORCS7* genes in iPSCs, we used the CRISPR–Cas9 system with a single guide RNA (sgRNA) per gene. For *BORCS5* KO, the sgRNA sequence was designed using Benchling (https://benchling.com) to target the second exon. We designed one forward and one reverse oligonucleotide bearing the selected sgRNA (uppercase) and the sequence necessary for cloning into the px458 plasmid (lowercase): forward 5′-caccgCTCAGGGCTCCCAGGCCTCA and reverse 5′-aaacTGAGGCCTGGGAGCCCTGAGc. For *BORCS7* KO, we used Benchling to design oligos bearing an sgRNA sequence targeting exon 1: forward 5′-caccgACGGAGAAGGTGACCACCTG and reverse 5′-aaacCAGGTGGTCACCTTCTCCGTc. Each of the guides was separately cloned into px458 plasmid (gift from F. Zhang, Addgene plasmid 48138). In brief, px458 plasmid was cut with BbsI, and the annealed oligonucleotides were inserted using T4 DNA ligase. The insertion was verified by sequencing. The plasmids bearing the sgRNAs were co-transfected into iPSCs using Lipofectamine 2000 (Thermo Fisher Scientific). Forty-eight hours later, single cells were sorted into 96-well plates based on GFP-positive signal. The single cells were allowed to grow in complete E8Flex medium supplemented with RevitaCell (A2644501, Thermo Fisher Scientific) for 1–2 weeks. When colonies were visible, cells were transferred to a six-well dish and grown until confluency. Cells were then harvested, and genomic DNA was isolated. PCR was conducted using forward 5′-AGTGACTCCTTCACCAGCCAAGCAT and reverse 5′-gtagagggaaagTAGTAGGGCTACAC primers for *BORCS5* and forward 5′-GGCCCCGGCGACTCACCATCGTCAG and reverse 5′-TACAATTCCCAAGATGCAACGCGAC primers for *BORCS7*. The PCR products were sequenced to verify the change from the WT sequence. Further verification was conducted by SDS-PAGE and immunoblotting with antibodies to BORCS5 or BORCS7 (Fig. 1c).

Lentivirus generation and rescue of KO cells

To rescue BORCS5-KO and BORCS7-KO cells, we used a lentiviral PGK-eGFP plasmid in which the human PGK promoter was substituted by the human EF1α promoter. The human BORCS5 or BORCS7-HA sequence was inserted after the promoter. A self-cleaving 2a peptide (P2A) was added between the BORC protein and the C-terminal eGFP. All these changes were carried out using Gibson Assembly (New England Biolabs). We also used site-directed mutagenesis to change glycine-2 to alanine in BORCS5, a mutation that was previously shown to prevent N-terminal myristoylation and association of BORCS5 with lysosomes[31]. Lentivirus was produced by co-expressing the obtained plasmid with psPAX2 (Addgene, 12260, gift of Didier Trono), pMD2.G (Addgene, 12259, gift of Didier Trono) and pAdVAntage Vector (Promega) in HEK293T cells using Lipofectamine 3000 (Thermo Fisher Scientific) according to the manufacturer's instructions. After 36 h, the virus-containing medium was spun at 700*g* for 5 min to remove cell debris and used to infect iPSCs for 36 h. iPSCs were then bulk sorted for GFP signal into a six-well plate. The GFP-positive cells were analyzed by SDS-PAGE and immunoblotting for BORCS5 or BORCS7 to verify the re-introduction of the corresponding protein (Fig. 1c).

Immunofluorescence microscopy

i3Neurons or primary mouse cortical neurons were seeded on polylysine–laminin-coated 18-mm coverslips or microfluidic devices. Neurons were then fixed in 4% w/v paraformaldehyde (Electron Microscopy Sciences) in PBS for 20 min and permeabilized-blocked with 0.1% w/v saponin and 1% w/v BSA (Gold Bio) in PBS for 20 min. Cells were sequentially incubated with primary and secondary antibodies diluted in 0.1% w/v saponin, 1% w/v BSA in PBS for 30 min at 37 °C (coverslips) or overnight at 4 °C with gentle oscillation (microfluidic devices). Cells were washed three times in PBS. Coverslips were mounted on glass slides

using Fluoromount-G (Electron Microscopy Sciences) with DAPI. For the devices, the Fluoromount-G–DAPI was added directly to the cells. *z*-stack cell images were acquired on a Zeiss LSM 880 inverted confocal microscope (Carl Zeiss) using a Plan-Apochromat ×63 objective (numerical aperture (NA) = 1.4). Maximum intensity projections were generated with Zeiss ZEN Black software, and final composite images were created using ImageJ/Fiji (https://fiji.sc/).

SDS-PAGE and immunoblotting

SDS-PAGE and immunoblotting methods are described in detail in Supplementary Data 1.

Microfluidic devices

The fabrication of microfluidic devices is described in detail in Supplementary Data 1.

Plating and culturing of i3Neurons in the microfluidic devices

The i3Neurons pre-differentiated for 3 d as described above were lifted with Accutase and counted. Cells (500,000) were plated in both lateral reservoirs ('neuron' compartments; Fig. 2a) of a microfluidic device bonded to a coverslip and pre-coated with polylysine-laminin. Every 3 d, half the medium was removed, and an equal volume of fresh medium was added to maintain neuronal health.

RNA preparation and sequencing

Samples from the neuronal and axonal compartments of the microfluidic devices were isolated with an RNeasy Micro Kit (Qiagen) according with the manufacturer's protocol for purification of total RNA from human cells. In brief, RNA from three axonal or neuronal compartments was extracted using a total of 100 µl of the kit's extraction buffer. No residual axons or cells were observed in the chamber after extraction. No carrier RNA was used for the extraction. On-column DNase digestion was performed. The RNA was eluted from the columns with 10 µl of RNase-free water. Then, 5 µl for axon samples and 1 µl for neuron samples were used for synthesizing cDNAs using a SMART-Seq version 4 Ultra Low Input RNA Kit for Sequencing (Takara). A Nextera XT DNA Library Preparation Kit (Illumina) was used to prepare libraries from the cDNA samples using 1 ng of cDNA. Libraries were run on a NovaSeq (SP Kit version 1.5, 200 cycles). Approximately 1 billion 2×100-bp reads were obtained with sequencing.

Bioinformatic analyses

Sequenced reads were aligned to GRCh38 human reference GENCODE release 28 using STAR (one-pass) version 2.7.8a[79]. Aligned reads were quantitated using the featureCounts function of the subread package version 2.0.1 (ref. 80) with GRCh38 human reference GENCODE release 28. After removing outliers, two WT axons, two WT neurons, three BORCS5-KO axons and three BORCS5-KO neurons were used as biological replicates for downstream differential expression analysis in R version 4.0.3. Differential expression analysis was performed using DESeq2 version 1.30.1 (ref. 81) by setting the model to '~celltype + 0' for axon versus neuron comparison in identical genotypes or '~genotype + 0' in identical cell types (for example, axon and neuron). The interaction term was modeled by '~celltype + genotype + celltype:genotype + 0' to compute differentially expressed genes (DEGs) in axons compared to neurons specifically to BORCS5 KO. $\log_2$ fold changes were computed using 'normal' and 'ashr' shrinkage in contrasts with and without an interaction term, respectively. DEGs were determined using a false discovery rate (FDR) cutoff of less than 10%.

The number of genes detected per sample was calculated using raw read counts, considering any genes with non-zero read counts in any replicate to be detected. The proportion of protein-coding, ribosomal, mitochondrial ribosomal and other RNA was assessed by matching gene biotypes and gene IDs using the ensembldb version 2.14.0 (ref. 82) *Homo sapiens* release ID AH89180 with normalized read counts. MA plots for protein-coding genes were created by plotting mean normalized read counts across the biological replicates on *x* axis and shrunken $\log_2$ fold changes on *y* axis.

To identify enriched gene sets, functional enrichment analysis on DEGs (FDR < 0.1) was conducted using the functions enrichGO and enrichKEGG from clusterProfiler version 4.8.3 (ref. 83). Enrichment dot plots and map were created using the shake_enrichResult, gs_summary_overview and distill_enrichment functions from GeneTonic version 1.5.2 (ref. 84). The dot plots were designed to display $-\log_{10}$ adjusted *P* values that were computed by enrichGO or enrichKEGG on *x* axis and z-scored by color. The z-scores were calculated by subtracting the number of down genes ($\log_2$ fold change < 0) from the number of up genes ($\log_2$ fold change > 0) and dividing the result by the square root of the total number of genes that have changed expression (either up or down). Enriched gene sets in contrasts with an interaction term were computed by performing functional enrichment analysis on DEGs from the interaction contrast that were also not differentially expressed in BORCS5-KO neurons compared to WT neurons.

Visualization of RNA particle and lysosome movement in the axon

WT and KO iPSCs were co-transfected with a plasmid encoding the PP7 coat protein followed by three HaloTags separated by GB1 domains and an in-house Super PiggyBac Transposase (https://doi.org/10.17504/protocols.io.q26g744b1gwz/v1) to ensure stable genomic integration of the HaloTag PP7 coat construct. The cells were allowed to recover in E8Flex medium for at least 1 d before they were passaged and expanded for 3 d. Expanded cells were lifted with Accutase, and, after replating, they were co-transfected again with a plasmid encoding SunTag-*RPS7* or *RPS27A* tagged with 24 PP7 repeats after their 3′ untranslated region (UTR) and the Super PiggyBac Transposase. The polyclonal, stable iPSCs were expanded, differentiated into i3Neurons and plated on 18-mm coverglasses pre-coated with polylysine and laminin as described above. After 15 d in culture, cells were transduced for 36 h with a lentivirus expressing the human LAMP1 protein fused with the monomeric NeonGreen fluorescent protein (LAMP1-mNeonGreen) under the control of the human PGK promoter. In some experiments, cells were similarly transduced with a lentivirus encoding human LAMP1 appended with three repeats of the kinesin-binding sequence (KBS) TNLEWDDSAI from PLEKHM2 (LAMP1–3×KBS)[31,47], followed by monomeric NeonGreen fluorescent protein (LAMP1–3×KBS-mNeonGreen). Alternatively, the polyclonal, stable iPSCs were expanded and differentiated into i3Neurons as spheroids. For spheroid differentiation, 10,000 iPSCs were lifted with Accutase and resuspended in 20 µl of differentiation medium per sphere. The iPSC suspension (20 µl) was added to a well of an ultra-low-attachment round-bottom 384-well plate (Corning) coated with anti-adherence solution (Life Technologies) for 1 h and washed with PBS three times. Cells were left to sit for 5 min before centrifuging at 540*g* for 2 min to help cells aggregate. The next day, 60 µl of induction medium was added. The third day after addition of induction medium to the 384-well plated cells, spheres were lifted by pipetting with a wide-bore, low-attachment pipette tip. Cells were then re-plated on a four-chamber glass-bottom slide (ibidi) coated with polylysine, followed by a 2-h coating with 15 µg ml^{-1} laminin and supplemented with 250 µl of neuronal culture medium. The day after re-plating, a full medium change was performed, followed by a half medium change 3 d after replating. The spheroids were imaged 1 week after re-plating. For live imaging of i3Neurons in coverslips, cells were incubated overnight with 200 pM of the Halo substrate JF646 (Promega, GA1120), and the axons were imaged live for 60 s (200-ms exposure time, no delay between images) on a spinning disk confocal microscope using a humidified environmental chamber. Alternatively, axons spreading outwards from the spheroids were imaged for 60 s (200-ms exposure time, no delay between images). Imaging of spheroids was focused on

an area with clear growth cones and relatively sparse axons to reduce the number of axons crossing over one another.

puro-PLA
The puro-PLA assay is described in detail in Supplementary Data 1.

Detection of mRNA using RNAscope ISH
The detection of mRNA using RNAscope ISH assay is described in detail in Supplementary Data 1.

Measurement of mitochondrial membrane potential and ROS
WT, BORCS5-KO and BORCS7-KO i3Neurons were grown on coverslips for 25 d. To detect the mitochondrial membrane potential (ΔΨm), i3Neurons were stained for 10 min at 37 °C with 50 nM of the ΔΨm-sensitive, fluorescent dye TMRE[85]. As a positive control, we pre-incubated WT i3Neurons for 5 min with 5 µM of the OXPHOS uncoupler carbonyl cyanide-4 (trifluoromethoxy) phenylhydrazone (FCCP) diluted in complete BrainPhys medium. To examine the levels of ROS, we stained i3Neurons for 10 min at 37 °C with 5 µM of the superoxide indicator dye MitoSOX[86] diluted in complete BrainPhys medium. As a control, we pre-treated WT i3Neurons for 5 min with 1 µM of the mitochondrial complex I inhibitor rotenone. After the incubations, neurons were washed twice with pre-warmed complete BrainPhys medium and imaged live using a Zeiss LSM 780 inverted confocal microscope (Carl Zeiss) fitted with a Plan-Apochromat ×63 objective (NA = 1.4). The microscope was equipped with a humidified environmental chamber kept at 37 °C and 5% CO_2 to maintain the cells during live imaging.

Quantification of mitochondria size
The quantification of mitochondrial size is described in detail in Supplementary Data 1.

Electron microscopy
Electron microscopy methods are described in detail in Supplementary Data 1.

Immunofluorescence microscopy of mouse sciatic nerves
Sciatic nerves were harvested from E17 WT and BORCS5-KO mouse embryo littermates. Nerves were then fixed for 2 h at 4 °C with 4% paraformaldehyde with gentle agitation. Nerves were permeabilized and blocked overnight with 0.1% w/v saponin and 1% w/v BSA (Gold Bio) in PBS. Nerves were sequentially incubated with primary and secondary antibodies diluted in 0.1% w/v saponin and 1% w/v BSA in PBS overnight at 4 °C with gentle agitation. Nerves were washed three times in PBS for 1 h each and mounted on glass slides using Fluoromount-G–DAPI (Electron Microscopy Sciences). Images were acquired on a Zeiss LSM 880 inverted confocal microscope (Carl Zeiss) using a Plan-Apochromat ×63 objective (NA = 1.4). Final composite images were created using ImageJ/Fiji (https://fiji.sc/).

Mouse cortical neuron transfection
The transfection of mouse cortical neurons is described in detail in Supplementary Data 1.

Live imaging of axonal microtubules and mitochondria
WT and KO i3Neurons, and mouse primary cortical neurons, were grown on coverslips for 25 d and 7 d, respectively. Neurons were incubated with SPY650-tubulin (Cytoskeleton, CY-SC503) (1:1,000) in culture medium for 1 h and MitoTracker Green (Thermo Fisher Scientific, M7514) (100 nM) for 10 min at 37 °C. Neurons were washed with pre-warmed culture medium and placed in an environmental chamber at 37 °C and 5% CO_2 on a Zeiss LSM 880 confocal microscope. Images were taken immediately using Airyscan mode with *z*-stacks and a Plan Apochromat ×63 objective (NA = 1.40).

Quantification of axonal degeneration
Primary cortical neurons from WT and BORCS5-KO mice were cultured for 10 d on glass coverslips. Phase-contrast light microscopy was used to capture images of axonal regions, identified by their thin diameter and absence of somas. The axon degeneration index (DI) was calculated as described previously[87]. In brief, phase-contrast images were visualized using Fiji, and then the image was transformed into a binary image. Axonal area was marked using the threshold function and measured (total axonal area), followed by particle analysis of the area occupied by fragmented axons. The DI was calculated dividing the area occupied by fragmented axons by the total axonal area.

Statistics and reproducibility
Quantified data were analyzed using Prism 9 (GraphPad Software). All bar graphs in the figures represent the mean ± s.d. from multiple determinations. When analyzing groups of data, the results are represented as SuperPlots[77] showing the individual data points in different colors, the mean from each experiment and the mean ± s.d. of the means. Each experiment was replicated at least three times on different days. The statistical significance of differences between two conditions was calculated using Student's *t*-test. The statistical significance for groups was calculated by one-way ANOVA with multiple comparisons using Dunnett's or Tukey's test as indicated in the figure legends. Significance is denoted using asterisks: $^{*}P < 0.05$, $^{**}P < 0.01$ and $^{***}P < 0.001$. $P > 0.05$ is not significant (NS). The total number of samples (*n*) analyzed in each experiment is indicated in the figure legends.

No statistical methods were used to predetermine sample sizes, but our sample sizes are similar to those reported in previous publications[15,16]. Instead, multiple independent experiments were carried out using several sample replicates as detailed in the figure legends. Data collection was not randomized. Data distribution was assumed to be normal, but this was not formally tested.

Data collection and analysis were not performed blinded to the conditions of the experiments.

Reporting summary
Further information on research design is available in the Nature Portfolio Reporting Summary linked to this article.

Data availability
Reagents generated in this study are available upon reasonable request. All data are available in the main text or Supplementary Information. Further information and requests for resources and reagents should be directed to the corresponding author. Bulk RNA-seq data have been deposited at GSE225479 and are publicly available as of the date of publication. Accession numbers are listed in the key resources table. Microscopy data reported in this paper will be shared by the lead contact upon reasonable request. Source data are provided with this paper.

Code availability
This paper does not report original code. Any additional information required to reanalyze the data reported in this paper is available from the corresponding author upon reasonable request.

References
78. Farías, G. G., Britt, D. J. & Bonifacino, J. S. Imaging the polarized sorting of proteins from the Golgi complex in live neurons. *Methods Mol. Biol.* **1496**, 13–30 (2016).
79. Dobin, A. et al. STAR: ultrafast universal RNA-seq aligner. *Bioinformatics* **29**, 15–21 (2013).
80. Liao, Y., Smyth, G. K. & Shi, W. featureCounts: an efficient general purpose program for assigning sequence reads to genomic features. *Bioinformatics* **30**, 923–930 (2014).

81. Love, M. I., Huber, W. & Anders, S. Moderated estimation of fold change and dispersion for RNA-seq data with DESeq2. *Genome Biol.* **15**, 550 (2014).
82. Rainer, J., Gatto, L. & Weichenberger, C. X. ensembldb: an R package to create and use Ensembl-based annotation resources. *Bioinformatics* **35**, 3151–3153 (2019).
83. Yu, G., Wang, L. G., Han, Y. & He, Q. Y. clusterProfiler: an R package for comparing biological themes among gene clusters. *OMICS* **16**, 284–287 (2012).
84. Marini, F., Ludt, A., Linke, J. & Strauch, K. GeneTonic: an R/Bioconductor package for streamlining the interpretation of RNA-seq data. *BMC Bioinformatics* **22**, 610 (2021).
85. Ehrenberg, B., Montana, V., Wei, M. D., Wuskell, J. P. & Loew, L. M. Membrane potential can be determined in individual cells from the nernstian distribution of cationic dyes. *Biophys. J.* **53**, 785–794 (1988).
86. Robinson, K. M. et al. Selective fluorescent imaging of superoxide in vivo using ethidium-based probes. *Proc. Natl Acad. Sci. USA* **103**, 15038–15043 (2006).
87. Sasaki, Y., Vohra, B. P., Baloh, R. H. & Milbrandt, J. Transgenic mice expressing the Nmnat1 protein manifest robust delay in axonal degeneration in vivo. *J. Neurosci.* **29**, 6526–6534 (2009).

Acknowledgements

We thank N. Maio, C. Cepko, D. Trono and F. Zhang for kind gifts of reagents; the Eunice Kennedy Shriver National Institute of Child Health and Human Development (NICHD) Molecular Genomics Core for RNA sequencing; C. Dye and L. Yi at the NICHD Microscopy and Imaging Core for the use of their electron microscope and histology preparation assistance; and M. López-Ocasio and P. Dagur at the National Heart, Lung, and Blood Institute Flow Cytometry Core for cell sorting. We also thank B. Mietto for help with isolation of sciatic nerves; S. Parikh for help with preparation of microfluidic devices; and X. Zhu and D. Abebe for excellent technical assistance. This work was supported by the Intramural Programs of the NICHD (ZIA HD001607 to J.S.B. and ZIC HD008986 to R.K.D.) and the National Institute of Neurological Disorders and Stroke (to M.E.W.) and by a Postdoctoral Research Associate Training program grant from the National Institute of General Medical Sciences (FI2GM142475 to V.H.R). The funders had no role in study design, data collection and analysis, decision to publish or preparation of the manuscript.

Author contributions

R.D.P., S.G., M.E.W. and J.S.B. designed the study. R.D.P. and S.G performed most of the experiments. V.H.R., R.D.P. and S.G. performed visualization of RNA particle movement in the axon. R.D.P., M.E.W., P.R.S. and N.Y.M. designed and developed the new microfluidic device. M.S. and R.K.D. performed bioinformatic and statistical analysis of RNA-seq datasets. M.J. performed electron microscopy. J.S.B., M.E.W. and R.K.D supervised the study. R.D.P., S.G. and J.S.B. wrote the original draft of the paper. All authors reviewed and edited the paper before submission.

Competing interests

The authors declare no competing interests.

Additional information

Extended data is available for this paper at https://doi.org/10.1038/s41593-024-01619-1.

Supplementary information The online version contains supplementary material available at https://doi.org/10.1038/s41593-024-01619-1.

Correspondence and requests for materials should be addressed to Juan S. Bonifacino.

Peer review information *Nature Neuroscience* thanks Shawn Ferguson and the other, anonymous, reviewer(s) for their contribution to the peer review of this work.

https://doi.org/10.1038/s41593-024-01619-1

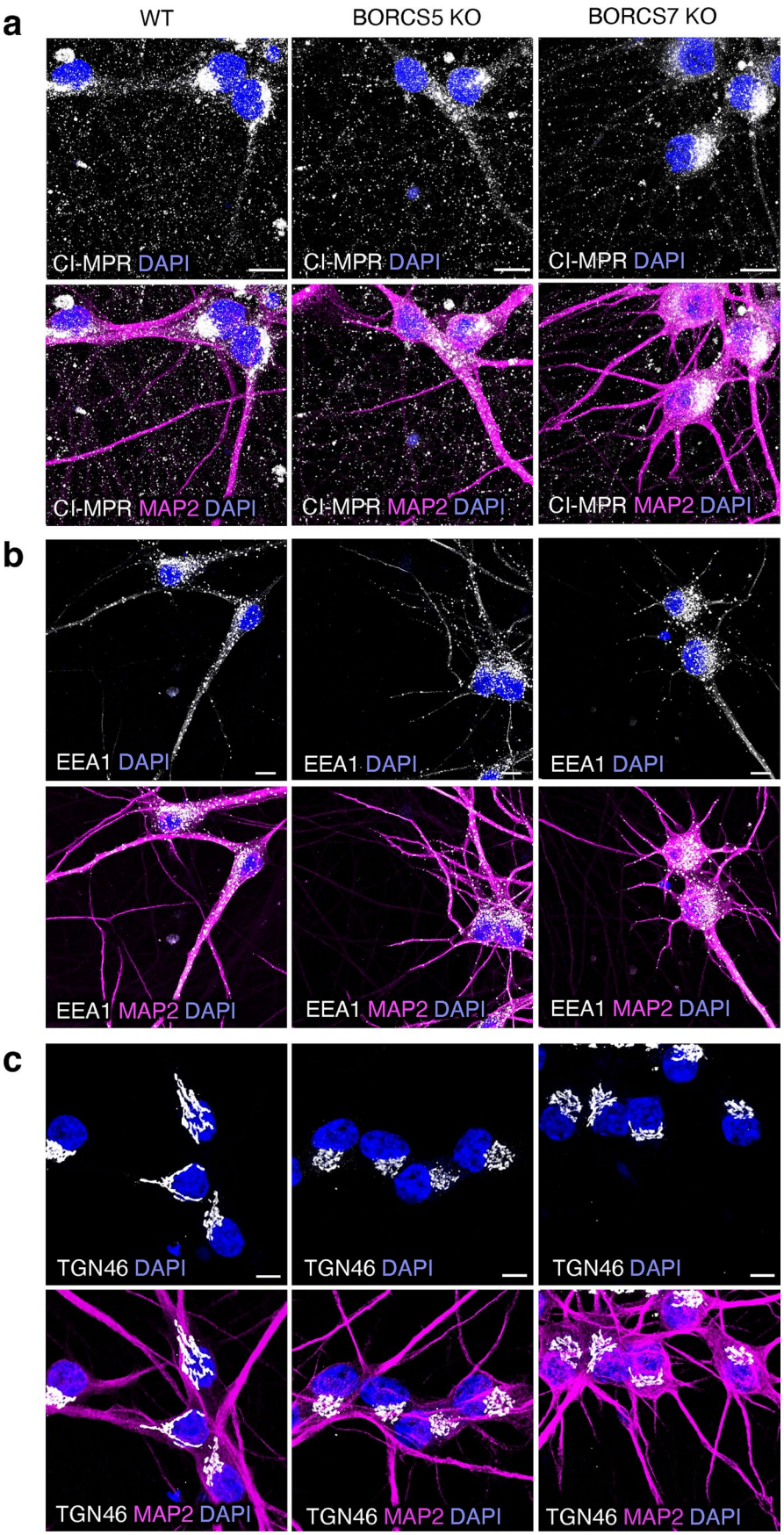

Extended Data Fig. 1 | See next page for caption.

https://doi.org/10.1038/s41593-024-01619-1

Extended Data Fig. 1 | Distribution of endosomal and TGN markers is not affected in BORC-KO i3Neurons. a-c, WT, BORCS5-KO and BORCS7-KO i3Neurons grown for 25 days on glass coverslips were fixed, permeabilized and co-stained with antibodies to endogenous MAP2 (soma and dendrites) (magenta) (all three panels) and cation-independent mannose 6-phosphate receptor (CI-MPR) (endosomes and TGN) (**a**), early endosomal antigen 1 (EEA1) (early endosomes) (**b**), or TGN46 (TGN) (**c**) (all in grayscale). Nuclear DNA was stained with DAPI (blue). Scale bars: 10 µm. Notice the presence of CI-MPR in all neuronal domains including axons (**a**), EEA1 only in the soma and dendrites (**b**) and TGN46 only in the soma (**c**), and how the distribution of all these markers does not change upon BORCS5 KO or BORCS7 KO. All the experiments shown in **a-c** were repeated three times.

https://doi.org/10.1038/s41593-024-01619-1

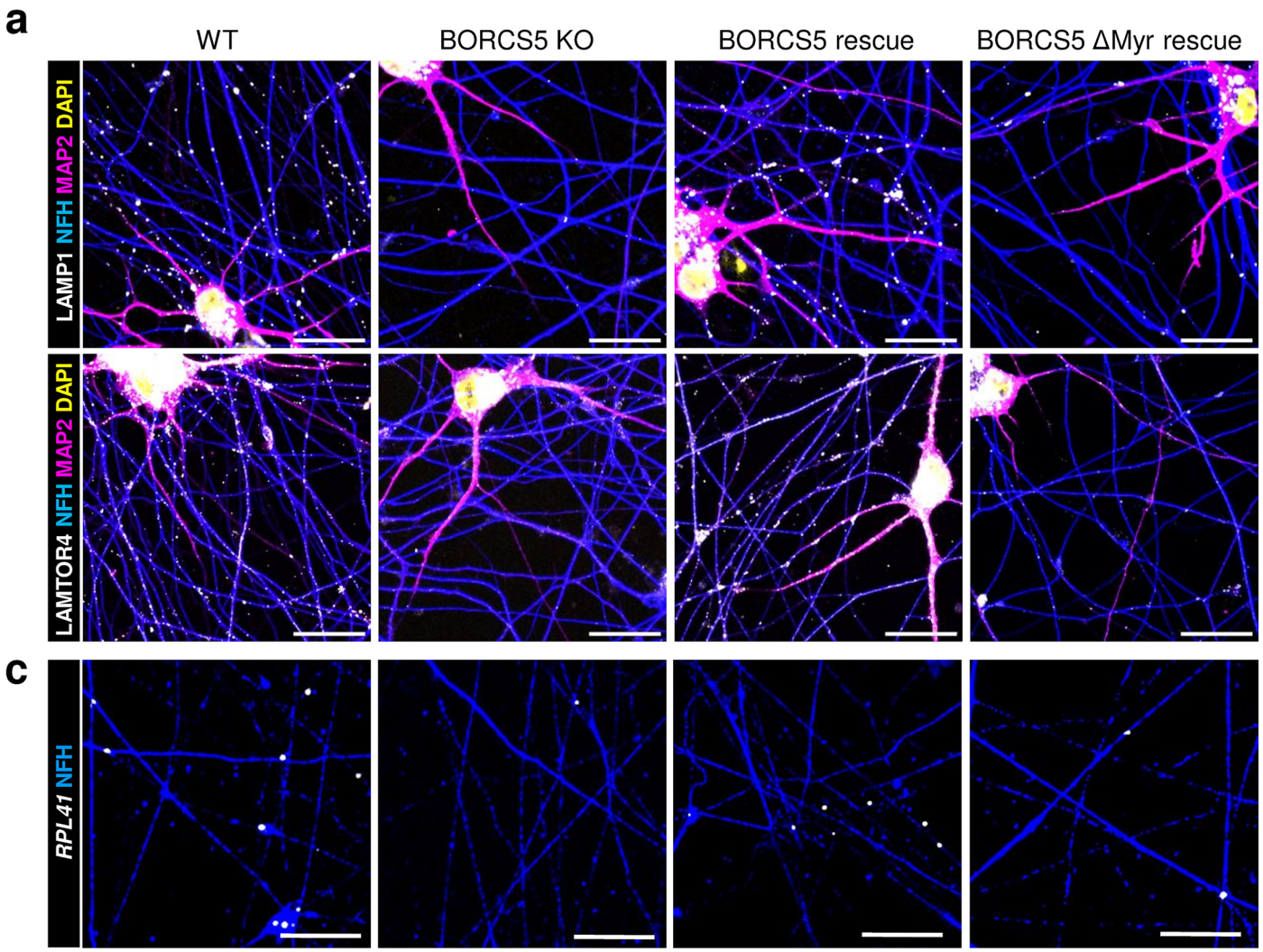

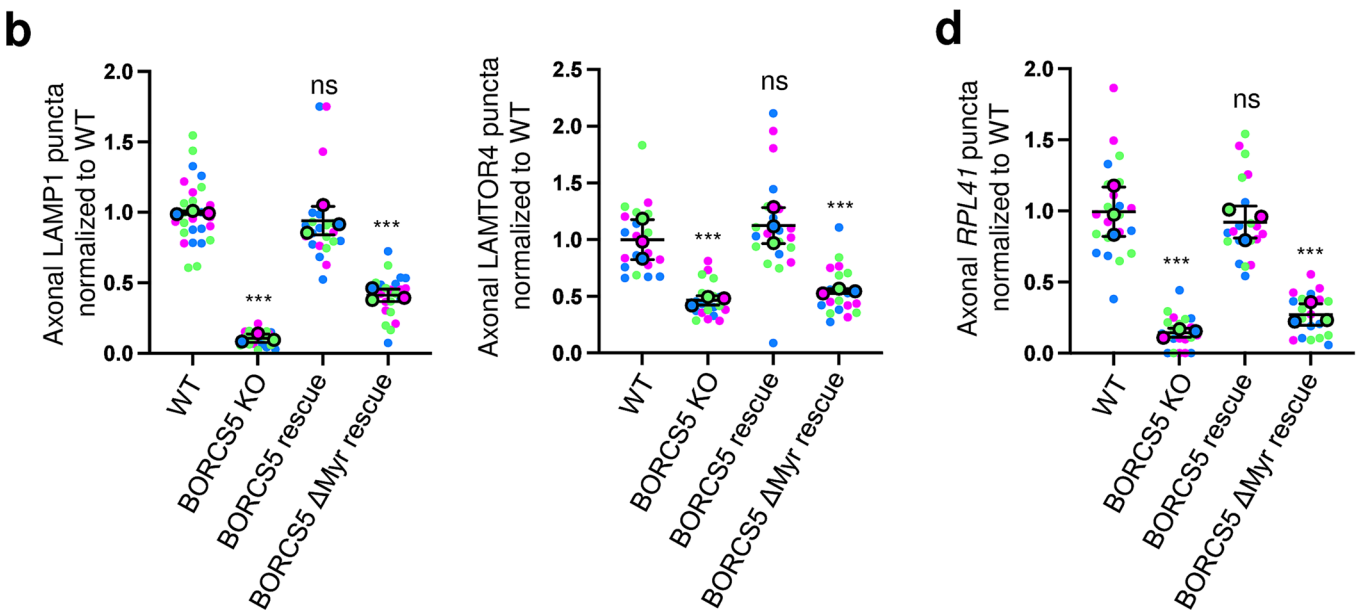

Extended Data Fig. 2 | See next page for caption.

https://doi.org/10.1038/s41593-024-01619-1

Extended Data Fig. 2 | Decreased *RPL41* mRNA staining in axons from BORCS5-KO i3Neurons. a, i3Neurons [WT, BORCS5 KO, BORCS5 KO rescued with WT BORCS5, and BORCS5 KO rescued with a G2A, myristoylation-defective BORCS5 (ΔMyr)] were immunostained for endogenous MAP2 (soma and dendrites) (magenta), neurofilament heavy chain (NFH) (axons, blue), LAMP1 (lysosomes) or LAMTOR4 (lysosomes) (all grayscale). Nuclei were stained with DAPI (yellow). Scale bars: 20 µm. Experiments were repeated three times. **b**, Quantification of the number of axonal puncta staining for LAMP1 or LAMTOR4 in the indicated i3Neuron lines relative to WT i3Neurons (defined as 1.0) from three experiments such as that shown in panel **a**. Results are represented as SuperPlots, showing the individual data points and mean of the means ± SD. Statistical significance was calculated by one-way ANOVA with Dunnett's multiple comparisons test. Significance relative to WT: LAMP1, BORCS5 KO ***$P < 0.001$, BORCS5 rescue $P = 0.586$, BORCS5 ΔMyr rescue ***$P < 0.001$. LAMTOR4, BORCS5 KO ***$P < 0.001$, BORCS5 rescue $P = 0.382$, BORCS5 ΔMyr rescue ***$P < 0.001$. ns: not significant. Notice the depletion of lysosome-related vesicles from the axon of BORCS5-KO neurons and the rescue of this phenotype by WT but not ΔMyr BORCS5. **c**, The same i3Neuron lines shown in panel **a** were grown on coverslips for 20 days, fixed and processed for RNAscope in situ hybridization using a probe for *RPL41* mRNA (white dots). Cells were also immunostained for NFH (axons, blue). Scale bars: 20 µm. Experiments were repeated three times. **d**, Quantification of the number of *RPL41* dots per axon unit area in the indicated i3Neuron lines relative to WT i3Neurons (defined as 1.0) from three experiments such as that shown in panel **c**. Results are represented as SuperPlots, showing the individual data points and mean of the means ± SD. Statistical significance was calculated by one-way ANOVA with Dunnett's multiple comparisons test. Significance relative to WT: *RPL41*, BORCS5 KO ***$P < 0.001$, BORCS5 rescue $P = 0.780$, BORCS5 ΔMyr rescue ***$P < 0.001$. Notice the depletion of *RPL41* mRNA in the axon of BORCS5-KO neurons, and the rescue of this phenotype by WT but not ΔMyr BORCS5, paralleling the results for lysosome-related vesicles.

https://doi.org/10.1038/s41593-024-01619-1

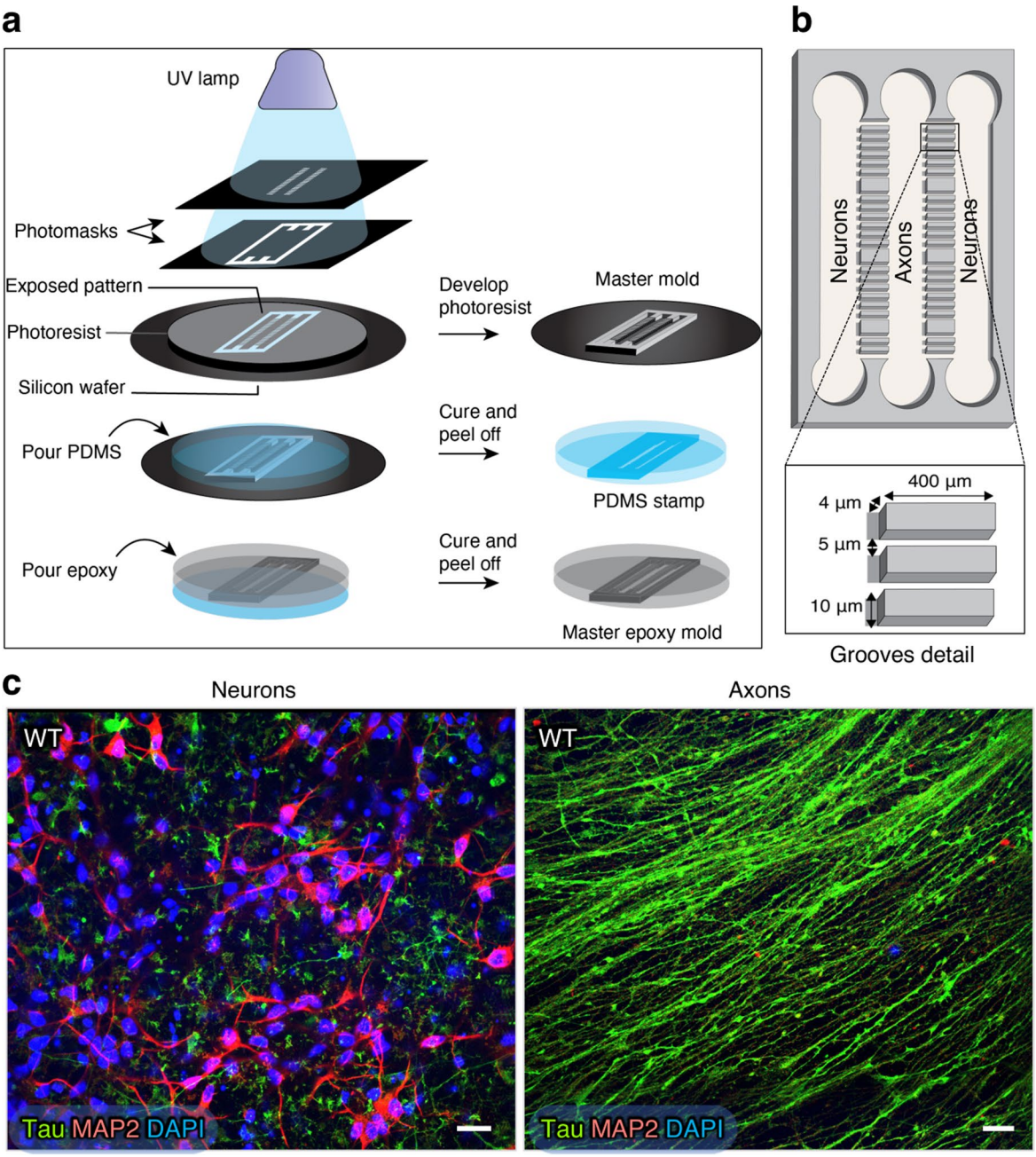

Extended Data Fig. 3 | Design of a microfluidic device for isolation of axons from i3Neurons. a, Schematic representation of the method used to prepare a microfluidic device. PDMS: polydimethylsiloxane. **b**, The device is composed of three open chambers approximately 2-mm wide by 40-mm long, separated by two sets of ~2,400 microgrooves with dimensions shown. A slightly wider gap (115 mm) between microgrooves is used every 1.7 mm to improve stability of the mounted device (see Supplementary Data 2 and 3 for CAD files of mask design). The PDMS component is represented in gray. Pre-differentiated i3Neurons are plated on the lateral chambers and axons grow into the middle chamber. This device provides a substantially larger culture area for neuronal seeding (400 mm^2 in the two outer chambers combined) and for axonal growth (200 mm^2 in the central chamber) compared to available commercial options. The open-chamber design provides an improved culture environment for the cells because it facilitates gas exchange with the medium and offers easier access for initial seeding, reagent addition, and sample collection. The high density of the microgrooves (60 microgrooves/mm), the ability to seed neurons close to the microgrooves, and the proximity of the entire area of the axon chamber to the microgrooves all help to increase the isolation throughput. **c**, WT i3Neurons grown for 45 days in a microfluidic device were immunostained for endogenous Tau (axons) and MAP2 (soma and dendrites). Nuclei were stained with DAPI. Images were obtained by confocal fluorescence microscopy. Representative images from the neuronal (left) or axonal (right) compartments are shown. Experiments were repeated three times. Notice the absence of somatodendritic and nuclear markers in the axonal compartment, indicating the purity of the axonal preparation. Scale bars: 20 µm.

https://doi.org/10.1038/s41593-024-01619-1

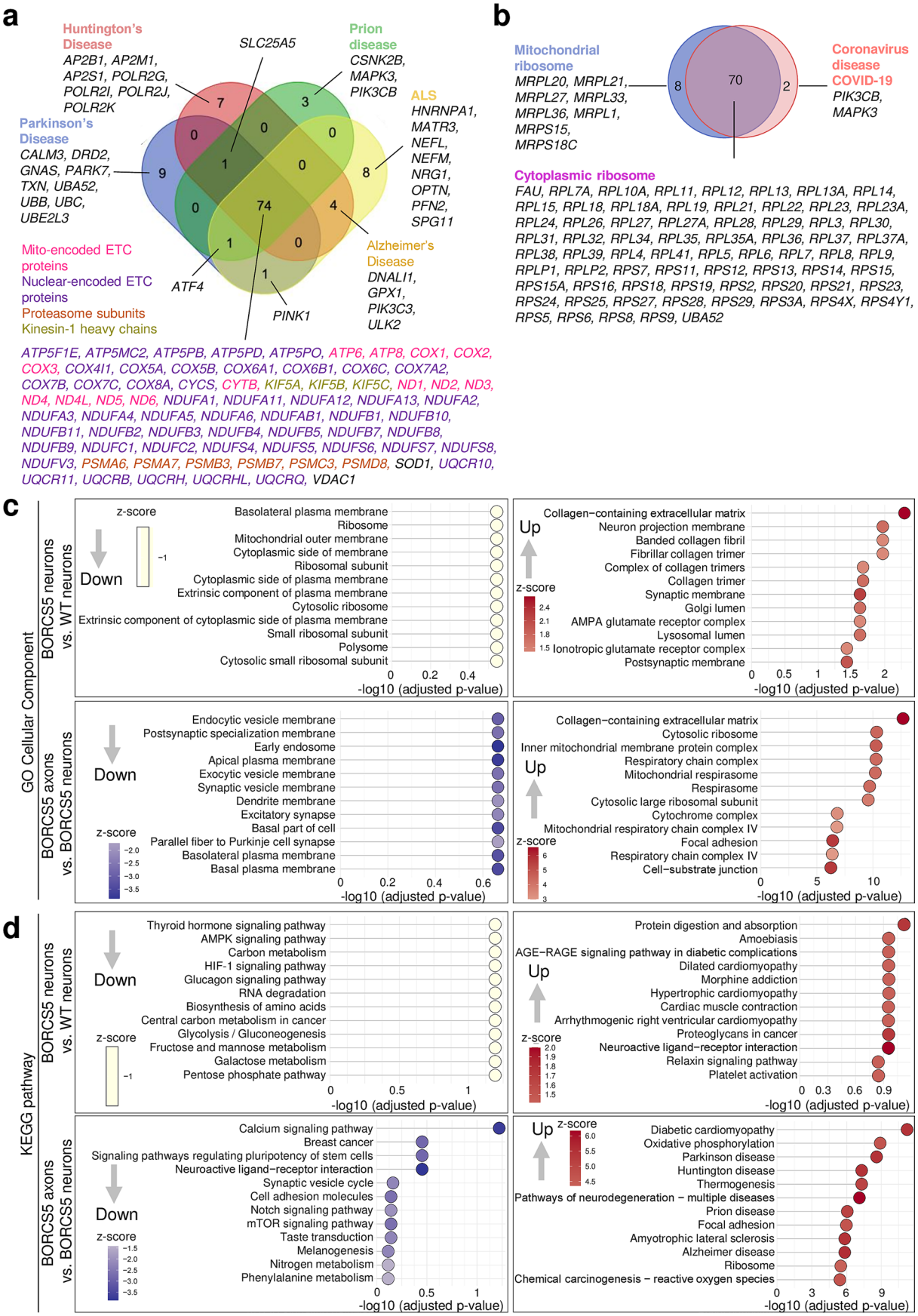

Extended Data Fig. 4 | See next page for caption.

https://doi.org/10.1038/s41593-024-01619-1

Extended Data Fig. 4 | Relationship of mRNA sets depleted in BORCS5-KO axons to neurodegenerative disorders and COVID-19, and GO Cellular Component and KEGG pathway analysis of changed mRNA sets. a, Venn diagram for functional enrichment related to neurodegenerative disorders. DEGs that were down in BORCS5-KO axons compared to WT axons matched to gene sets related to neurodegenerative disorders, as defined by KEGG. **b**, Venn diagram for functional enrichment related to ribosomes and COVID-19. DEGs that were down in BORCS5-KO axons compared to WT axons matched to gene sets related to ribosome and COVID-19, as defined by KEGG. **c**, GO Cellular Component analysis of gene sets that are increased or decreased in BORCS5-KO neurons vs WT neurons and BORCS5-KO axons vs BORCS5-KO neurons. **d**, KEGG pathway analysis of gene sets that are increased or decreased in BORCS5-KO neurons vs WT neurons and BORCS5-KO axons vs BORCS5-KO neurons. Both **c** and **d** show dot plots for DEG sets that are increased (up) or decreased (down) in RNA-Seq. Enriched terms are arranged by statistical significance (FDR), showing the top 12 terms. The z-score captures both the direction of changes and the number of genes changing in each direction. A larger absolute z-score indicates a more biased direction towards increase or decrease. Statistical significance was calculated by one-sided Fisher's exact test. *P*-values were adjusted for multiple comparisons using the Benjamini-Hochberg method.

https://doi.org/10.1038/s41593-024-01619-1

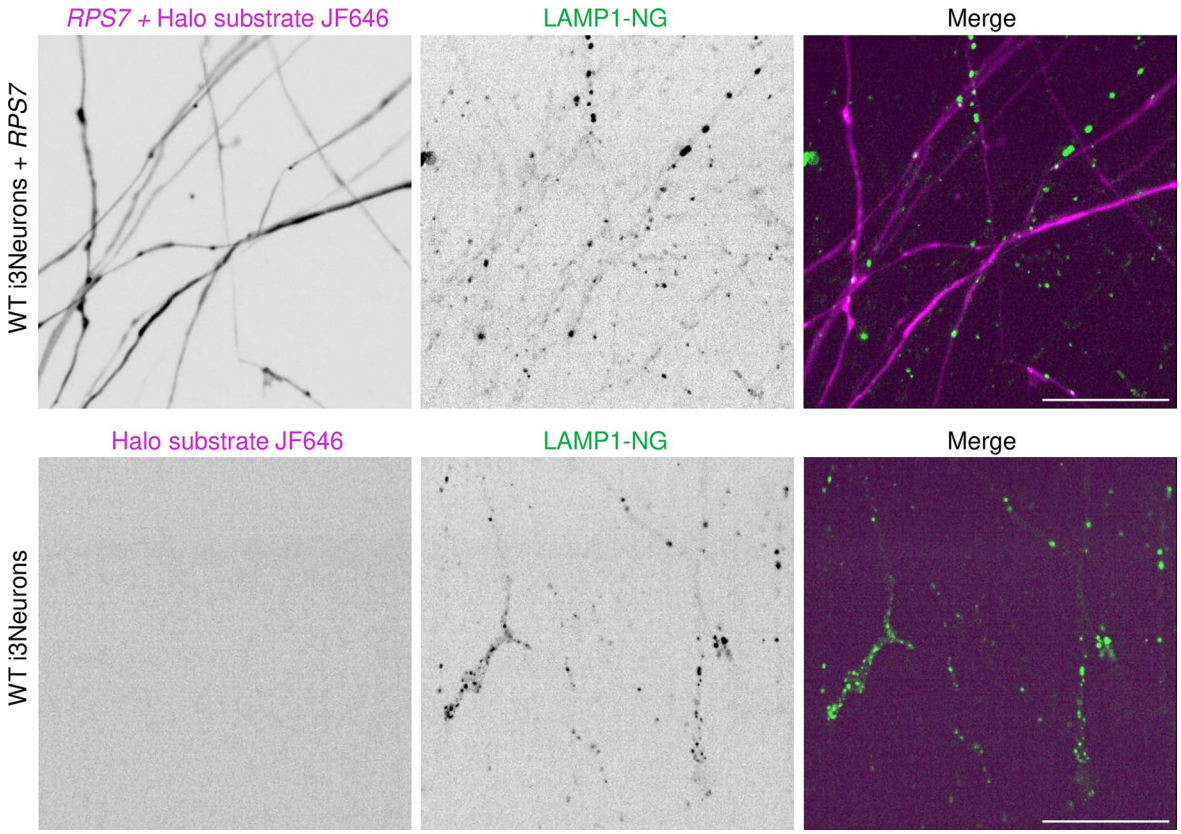

Extended Data Fig. 5 | Control experiment demonstrating the specificity of HaloTag staining in mRNA transport experiments. WT i3Neurons co-expressing 3 HaloTags fused to PP7 coat protein and *RPS7* fused to 24 PP7 RNA stem-loop repeats (top row) (see scheme in Fig. 4a), or untransfected WT i3Neurons (negative control) (bottom row), were grown on coverslips for 25 days and transduced with LAMP1-mNeonGreen (LAMP1-NG) for 36 h. Neurons were then incubated overnight with 200 pM of the fluorescent HaloTag substrate JF646 and imaged by spinning-disk confocal microscopy. Scale bars: 20 µm. Notice the absence of JF646 signal in the control i3Neurons, demonstrating that the JF646 signal represents *RPS7* staining and not non-specific staining of lysosome-related vesicles or other vesicles. Experiments were repeated three times.

https://doi.org/10.1038/s41593-024-01619-1

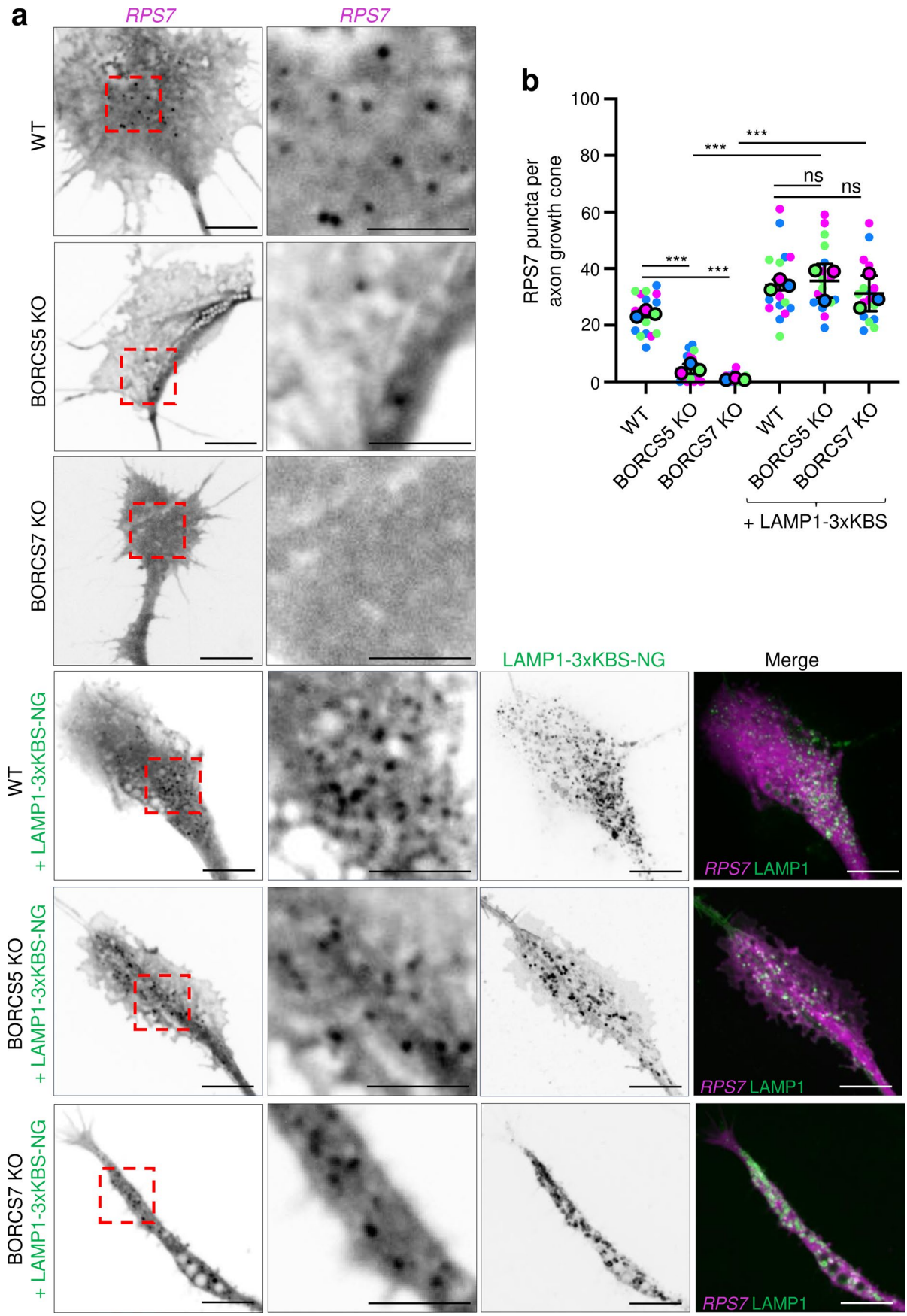

Extended Data Fig. 6 | See next page for caption.

https://doi.org/10.1038/s41593-024-01619-1

Extended Data Fig. 6 | BORC-independent rescue of axonal *RPS7* mRNA by expression of LAMP1-3xKBS in BORCS5-KO and BORCS7-KO i3Neurons. **a**, WT, BORCS5-KO and BORCS7-KO i3Neurons co-expressing the PP7 coat protein fused with three HaloTags and *RPS7* CDS fused with 24 PP7 RNA stem-loop repeats were grown on coverslips for 15 days. Cells were then transduced with a construct encoding three repeats of a kinesin-binding sequence (KBS) fused to NeonGreen-tagged LAMP1 (LAMP1-3xKBS-NG) for 36 h and incubated with 200 pM of the fluorescent Halo substrate JF646 overnight to image lysosome-related vesicles and *RPS7* mRNA localization at axon terminals. Scale bars for left, LAMP1-3xKBS-NG and merged columns: 10 µm. Scale bars for *RPS7* zoomed-in boxed areas: 5 µm. **b**, Quantification of the number of *RPS7* puncta per axon terminal from n = 3 independent experiments. Values are represented as SuperPlots, showing the individual data points and the mean of the means ± SD. Statistical significance was calculated by one-way ANOVA with Dunnett's multiple comparisons test. BORCS5 KO vs WT ***$P < 0.001$, BORCS7 KO vs WT ***$P < 0.001$, BORCS5 KO + LAMP1-3xKBS vs BORCS5 KO ***$P < 0.001$, BORCS7 KO + LAMP1-3xKBS vs BORCS7 KO ***$P < 0.001$, BORCS5 KO + LAMP1-3xKBS vs WT + LAMP1-3xKBS $P = 0.998$, BORCS7 KO + LAMP1-3xKBS vs WT + LAMP1-3xKBS $P = 0.949$. ns: not significant relative to WT. Notice the increased number of *RPS7* mRNA and lysosomal puncta in BORCS5-KO and BORCS7-KO i3Neurons transduced with LAMP1-3xKBS-NG.

https://doi.org/10.1038/s41593-024-01619-1

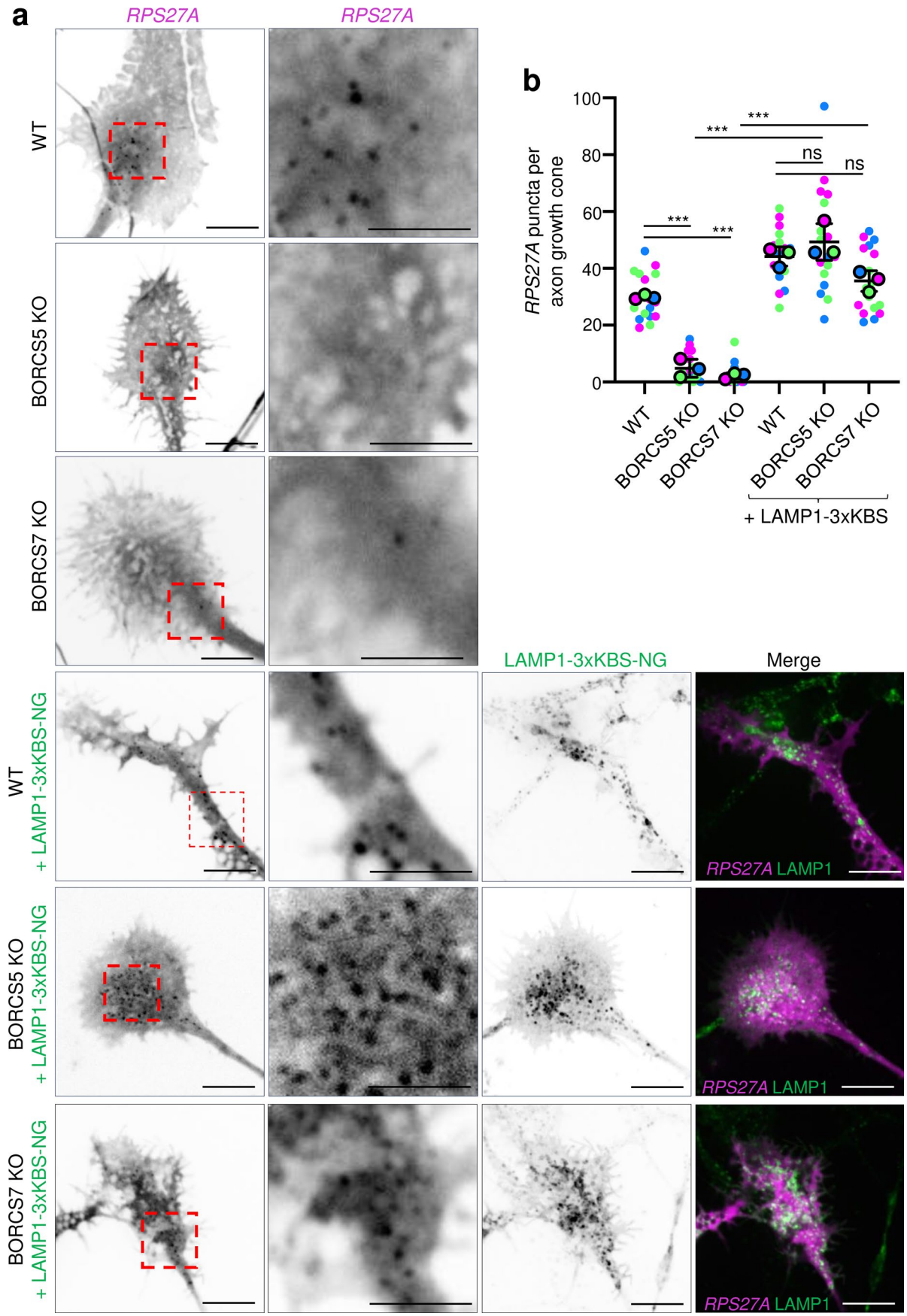

Extended Data Fig. 7 | See next page for caption.

https://doi.org/10.1038/s41593-024-01619-1

Extended Data Fig. 7 | BORC-independent rescue of axonal *RPS27A* mRNA by expression of LAMP1-3xKBS in BORCS5-KO and BORCS7-KO i3Neurons. **a**, WT, BORCS5-KO and BORCS7-KO i3Neurons co-expressing the PP7 coat protein fused with three HaloTags and *RPS27A* CDS fused with 24 PP7 RNA stem-loop repeats were grown on coverslips for 15 days. Cells were then transduced with a construct encoding LAMP1-3xKBS-NG for 36 h and incubated with 200 pM of the fluorescent Halo substrate JF646 overnight to image lysosome-related vesicles and *RPS27A* mRNA localization at axon terminals. Scale bars for left, LAMP1-3xKBS-NG and merged columns: 10 µm. Scale bars for *RPS27A* zoomed-in boxed areas: 5 µm. **b**, Quantification of the number of *RPS27A* puncta per axon terminal from n = 3 independent experiments. Values are represented as SuperPlots, showing the individual data points and the mean of the means ± SD. Statistical significance was calculated by one-way ANOVA with Dunnett's multiple comparisons test. BORCS5 KO vs WT ***$P < 0.001$, BORCS7 KO vs WT ***$P < 0.001$, BORCS5 KO + LAMP1-3xKBS vs BORCS5 KO ***$P < 0.001$, BORCS7 KO + LAMP1-3xKBS vs BORCS7 KO ***$P < 0.001$, BORCS5 KO + LAMP1-3xKBS vs WT + LAMP1-3xKBS $P = 0.721$, BORCS7 KO + LAMP1-3xKBS vs WT + LAMP1-3xKBS $P = 0.136$. ns: not significant relative to WT. Notice the increased number of *RPS27A* mRNA and lysosomal puncta in BORCS5-KO and BORCS7-KO i3Neurons transduced with LAMP1-3xKBS-NG.

https://doi.org/10.1038/s41593-024-01619-1

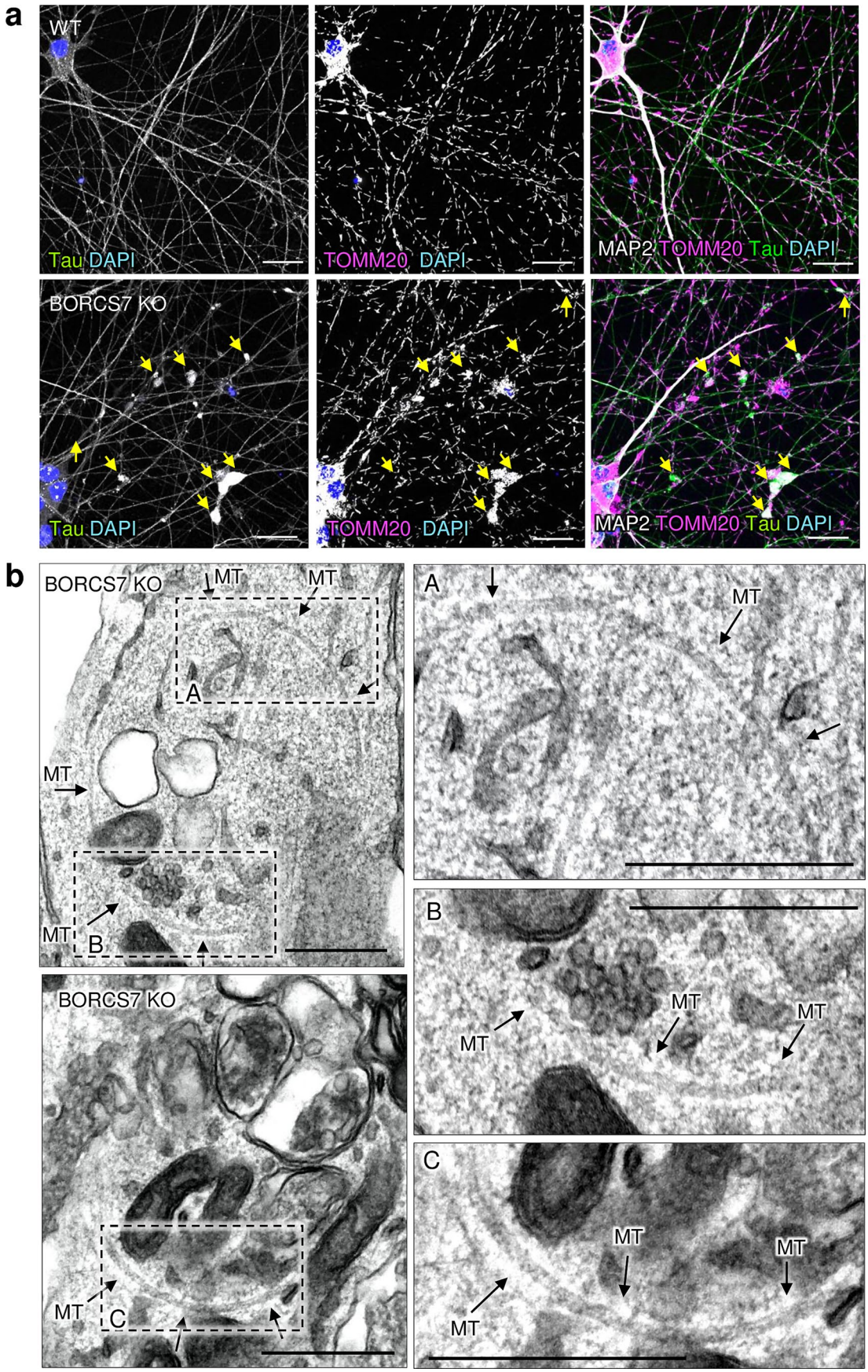

Extended Data Fig. 8 | See next page for caption.

https://doi.org/10.1038/s41593-024-01619-1

Extended Data Fig. 8 | Tau aggregates and microtubule swirls in axonal swellings from BORCS7-KO i3Neurons. a, WT and BORCS7-KO i3Neurons were cultured for 25 days on glass coverslips and stained with Tau-1 antibody (marker for axons and axonal degeneration when aggregated), TOMM20 (mitochondria), and MAP2 (soma and dendrites). Nuclei were stained with DAPI (blue). Neurons were imaged by confocal fluorescence microscopy. Notice that swellings in BORCS7-KO axons (yellow arrows) contain Tau-1-positive aggregates and mitochondria. Scale bars: 10 µm. Experiments were repeated three times. **b**, BORCS7-KO i3Neurons grown for 25 days on glass coverslips were analyzed by TEM. *Left column*: detailed view of two axonal swellings in BORCS7-KO axons. *Right column*: magnified views of the boxed areas on the left. Curved microtubules (MT) indicative of a swirl-like organization are visible in the swellings (arrows). Scale bars: 400 nm. This experiment was repeated twice.

https://doi.org/10.1038/s41593-024-01619-1

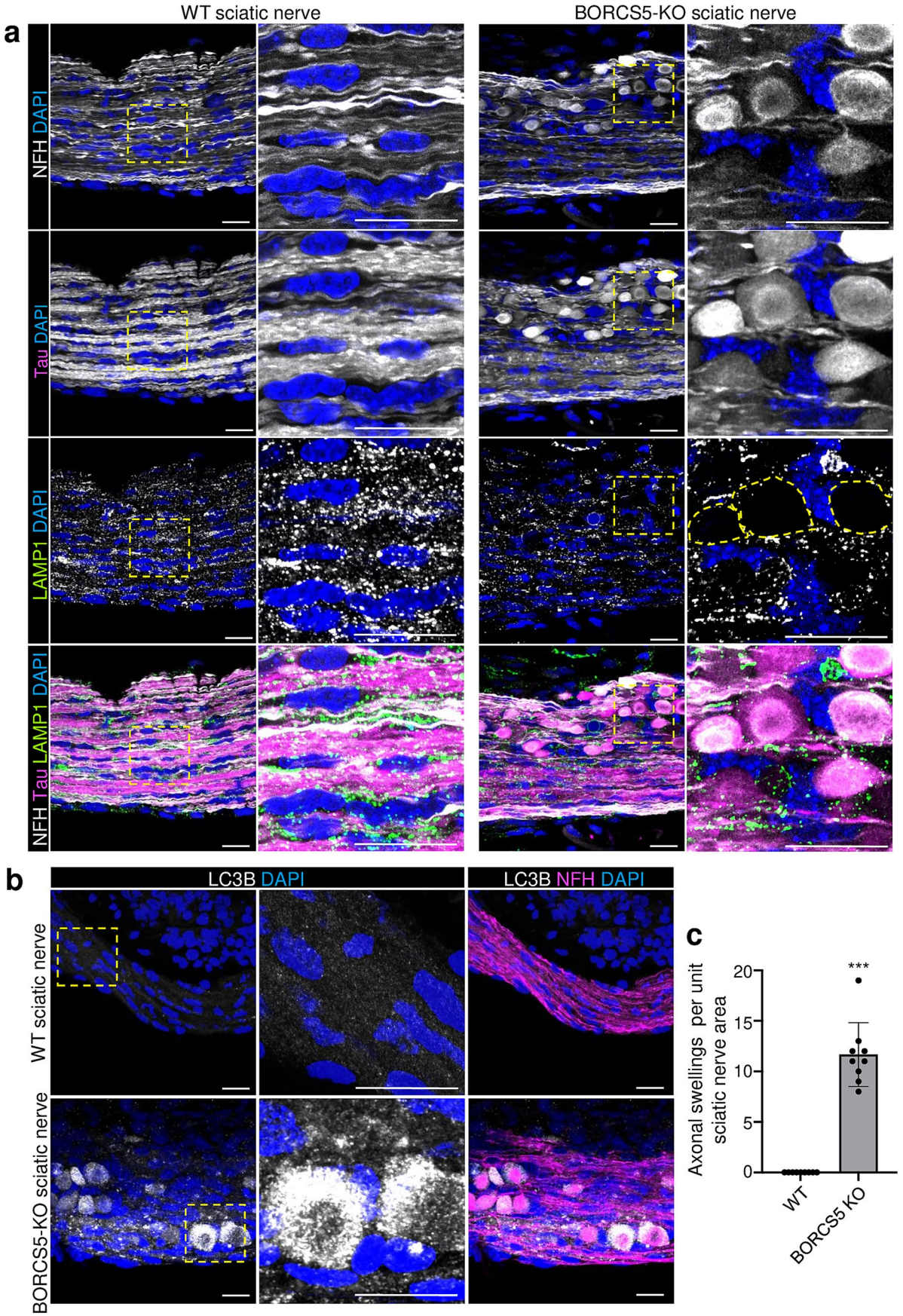

Extended Data Fig. 9 | See next page for caption.

https://doi.org/10.1038/s41593-024-01619-1

Extended Data Fig. 9 | Axonal swellings containing neurofilament protein, Tau, and autophagosomes in sciatic nerves from BORCS5-KO mice. **a**, **b**, Sciatic nerves were isolated from WT and BORCS5-KO E17 mouse embryos. Nerves were fixed and immunostained for endogenous Tau (magenta) and LAMP1 (lysosomes, green) (panel **a**) or LC3B (autophagosomes, grayscale) (panel **b**). Nerves were also co-stained for NFH (axons, grayscale in panel **a** and magenta in panel **b**), and DAPI (nuclei, blue), and imaged by confocal fluorescence microscopy. Enlarged views of the boxed areas are shown on the right. Areas encircled by dashed lines indicate swellings devoid of LAMP1 staining. Scale bars: 20 µm. **c**, Quantification of the number of axonal swellings (NFH-positive) per unit of sciatic nerve area from n = 9 images captured from n = 3 animals. Values are the mean ± SD from representative images like those shown in panels **a** and **b**. Statistical significance was calculated using an unpaired two-tailed Student's t test. BORCS5 KO vs WT ***$P < 0.001$.

https://doi.org/10.1038/s41593-024-01619-1

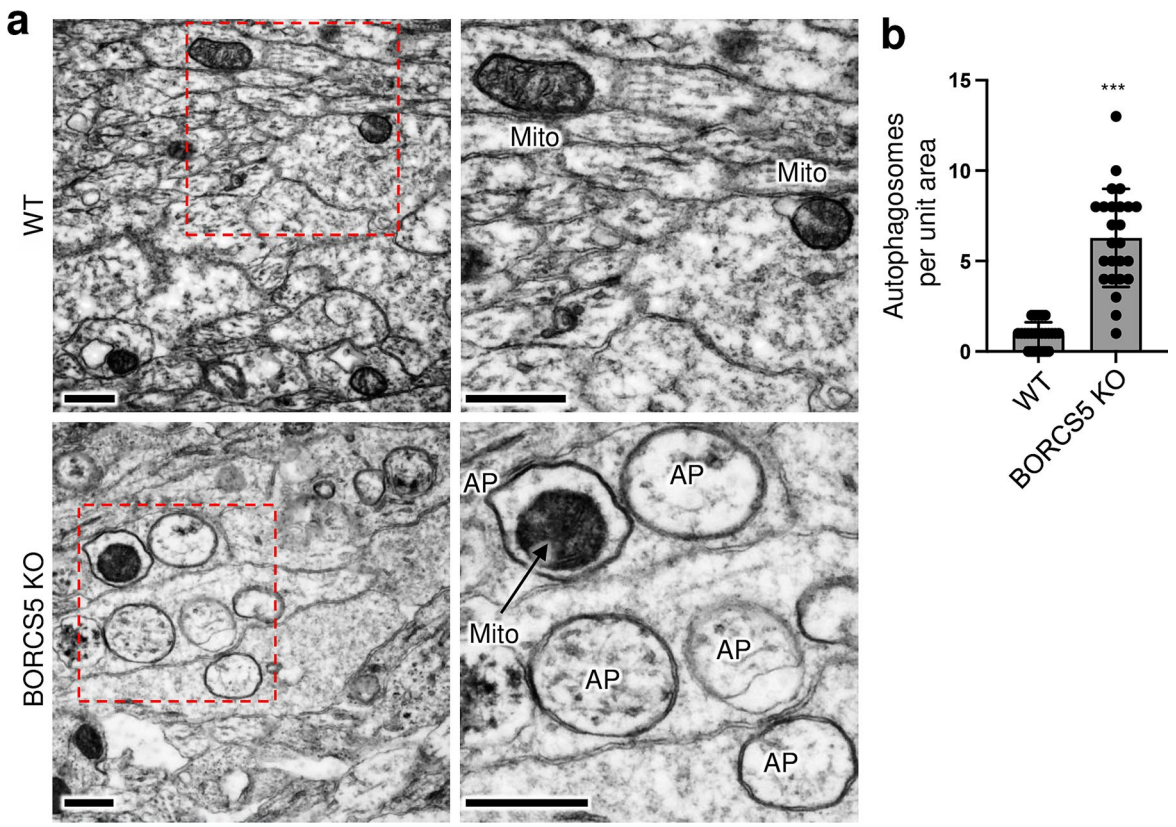

Extended Data Fig. 10 | Accumulation of autophagosomes in the axons of BORCS5 -KO mouse brain. a, Brains were harvested from WT and BORCS5-KO E17 mouse embryos and the corpus callosum was analyzed by TEM as described in the Methods. The figure shows low magnification (left column) and high magnification images of the boxed areas (right column). Notice the presence of numerous autophagosomes (AP) in the axons of BORCS5-KO neurons, morphologically identified by their size and presence of synaptic vesicles, microtubules, and neurofilaments. Scale bars: 600 nm. **b**, Quantification of the number of autophagosomes per field unit area from n = 25 images captured from n = 2 animals. Values are the mean ± SD from representative images like those shown in panel **a**. Statistical significance was calculated using an unpaired two-tailed Student's t test. BORCS5 KO vs WT ***$P < 0.001$.

nature portfolio

Corresponding author(s): Juan S. Bonifacino

Last updated by author(s): Mar 21, 2024

Reporting Summary

Nature Portfolio wishes to improve the reproducibility of the work that we publish. This form provides structure for consistency and transparency in reporting. For further information on Nature Portfolio policies, see our Editorial Policies and the Editorial Policy Checklist.

Statistics

For all statistical analyses, confirm that the following items are present in the figure legend, table legend, main text, or Methods section.

n/a	Confirmed	
☐	☒	The exact sample size (*n*) for each experimental group/condition, given as a discrete number and unit of measurement
☐	☒	A statement on whether measurements were taken from distinct samples or whether the same sample was measured repeatedly
☐	☒	The statistical test(s) used AND whether they are one- or two-sided *Only common tests should be described solely by name; describe more complex techniques in the Methods section.*
☒	☐	A description of all covariates tested
☐	☒	A description of any assumptions or corrections, such as tests of normality and adjustment for multiple comparisons
☐	☒	A full description of the statistical parameters including central tendency (e.g. means) or other basic estimates (e.g. regression coefficient) AND variation (e.g. standard deviation) or associated estimates of uncertainty (e.g. confidence intervals)
☐	☒	For null hypothesis testing, the test statistic (e.g. *F*, *t*, *r*) with confidence intervals, effect sizes, degrees of freedom and *P* value noted *Give P values as exact values whenever suitable.*
☒	☐	For Bayesian analysis, information on the choice of priors and Markov chain Monte Carlo settings
☒	☐	For hierarchical and complex designs, identification of the appropriate level for tests and full reporting of outcomes
☐	☒	Estimates of effect sizes (e.g. Cohen's *d*, Pearson's *r*), indicating how they were calculated

Our web collection on statistics for biologists contains articles on many of the points above.

Software and code

Policy information about availability of computer code

Data collection	Confocal images were acquired on a Zeiss LSM 880 inverted confocal microscope (Carl Zeiss) using a Plan-Apochromat 63X objective (NA=1.4). Maximum intensity projections were generated with Zeiss ZEN Black software, and final composite images were created using ImageJ/Fiji (https://fiji.sc/). Live cell imaging was performed on a spinning-disk Nikon confocal microscope using a humidified environmental chamber kept at 37°C and 5% CO2, or with a Zeiss LSM 780 inverted confocal microscope (Carl Zeiss) fitted with a Plan-Apochromat 63X objective (NA=1.4).

Data analysis	Fiji/ImageJ NIH https://fiji.sc/ RRID:SCR_002285 v2.9.0 IMARIS Oxford Instruments https://imaris.oxinst.com/ RRID:SCR_007370 v8.2.0 GraphPad Prism GraphPad http://www.graphpad.com/ RRID:SCR_002798 v9.5.0 SnapGene Dotmatics http://www.snapgene.com/ RRID:SCR_015052 v6.2.1 BioRender BioRender https://www.biorender.com/ RRID:SCR_018361 v2023 AutoCAD Autodesk https://web.autocad.com/login v2023 STAR https://github.com/alexdobin/STAR v2.7.8a featureCounts (subread) https://subread.sourceforge.net/ v2.0.1 R https://www.r-project.org/ v4.0.3 DESeq2 https://bioconductor.org/packages/release/bioc/html/DESeq2.html v1.30.1 ensembldb https://bioconductor.org/packages/release/bioc/html/ensembldb.html v2.14.0 clusterProfiler https://bioconductor.org/packages/release/bioc/html/clusterProfiler.html v3.18.1 GeneTonic https://bioconductor.org/packages/release/bioc/html/GeneTonic.html v1.5 Zen black https://www.micro-shop.zeiss.com/en/us/softwarefinder/software-categories/zenblack/ v14.0

For manuscripts utilizing custom algorithms or software that are central to the research but not yet described in published literature, software must be made available to editors and reviewers. We strongly encourage code deposition in a community repository (e.g. GitHub). See the Nature Portfolio guidelines for submitting code & software for further information.

Data

Policy information about availability of data

All manuscripts must include a data availability statement. This statement should provide the following information, where applicable:

- Accession codes, unique identifiers, or web links for publicly available datasets
- A description of any restrictions on data availability
- For clinical datasets or third party data, please ensure that the statement adheres to our policy

Reagents generated in this study are available upon request. All data are available in the main text or the supplementary materials. Further information and requests for resources and reagents should be directed to the lead contact, Juan S. Bonifacino (juan.bonifacino@nih.gov). Bulk RNA-Seq data have been deposited at GSE225479, and are publicly available as of the date of publication. Accession numbers are listed in the key resources table. Microscopy data reported in this paper will be shared by the lead contact upon request.

Research involving human participants, their data, or biological material

Policy information about studies with human participants or human data. See also policy information about sex, gender (identity/presentation), and sexual orientation and race, ethnicity and racism.

Reporting on sex and gender	N/A
Reporting on race, ethnicity, or other socially relevant groupings	N/A
Population characteristics	N/A
Recruitment	N/A
Ethics oversight	N/A

Note that full information on the approval of the study protocol must also be provided in the manuscript.

Field-specific reporting

Please select the one below that is the best fit for your research. If you are not sure, read the appropriate sections before making your selection.

☒ Life sciences ☐ Behavioural & social sciences ☐ Ecological, evolutionary & environmental sciences

For a reference copy of the document with all sections, see nature.com/documents/nr-reporting-summary-flat.pdf

Life sciences study design

All studies must disclose on these points even when the disclosure is negative.

Sample size	No statistical methods were used to predetermine sample sizes, but our sample sizes are similar to those reported in previous publications. (Maday et al. 2012; Cheng et al. 2015). Instead, multiple independent experiments were carried out using several sample replicates as detailed in the figure legends.
Data exclusions	Biological replicate #3 from WT Neurons and biological replicate #3 from WT Axons were outliers and therefore removed from for downstream differential expression analysis. This is specified in the text, in the Bioinformatic analyses section.

Replication	Multiple independent experiments were carried out using several sample replicates as detailed in the figure legends. All replication attempts were successful.
Randomization	No randomization was used when comparing i3Neurons wildtype and KO since treatment group of cells were generally derived from the same population of cells. For primary neuron analysis, animals from different litters were used for repeat experiments. Comparisons between KO and wildtype controls were made from neurons harvested within the same litter. In this study, animals were allocated into experimental groups based on genotype, so randomization was not applicable. For immunohistochemistry variation, animals or cells for the same experiment were always processed on the same day, using the same reagents, and were collected on the same slides for staining. Imaging parameters were held constant across the same experiment.
Blinding	A strategy for randomization, stratification or blind selection of samples was not carried out. Comparison between wildtype and KO neurons were not blinded for practical reasons as too few investigators were involved in the study.

Reporting for specific materials, systems and methods

We require information from authors about some types of materials, experimental systems and methods used in many studies. Here, indicate whether each material, system or method listed is relevant to your study. If you are not sure if a list item applies to your research, read the appropriate section before selecting a response.

Materials & experimental systems

n/a	Involved in the study
☐	☒ Antibodies
☐	☒ Eukaryotic cell lines
☒	☐ Palaeontology and archaeology
☐	☒ Animals and other organisms
☒	☐ Clinical data
☒	☐ Dual use research of concern
☒	☐ Plants

Methods

n/a	Involved in the study
☒	☐ ChIP-seq
☒	☐ Flow cytometry
☒	☐ MRI-based neuroimaging

Antibodies

Antibodies used

Primary antibodies:
BORCS5 (LOH12CR1), rabbit, used 1:500 for IB Proteintech Cat#17169-1-AP, RRID:AB_2137150
BORCS7 (C10orf32), rabbit, used 1:500 for IB Abnova Cat#PAB23142, RRID:AB_11122571
GAPDH (0411) HRP conjugated, used 1:1,000 for IB Santa Cruz Cat#sc-47724, RRID:AB_627678
Alpha-tubulin, mouse, used 1:5,000 for IB Santa Cruz Cat#sc-32293
RRID:AB_628412
LAMP1, mouse, used 1:500 for IF Developmental Studies Hybridoma Bank Cat#H4A3, RRID:AB_2296838
LAMP1, rat, used 1:500 for IB Developmental Studies Hybridoma Bank Cat#1D4B, RRID:AB_2134500
MAP2, chicken, used 1:1,000 for IB, 1:500 for IB Abcam Cat#ab5392, RRID:AB_2138153
MAP2 (H-300), rabbit, used 1:500 for IF Santa Cruz Cat#sc-20172, RRID:AB_2250101
Synaptophysin 1 (SYP1) (D-4), mouse, used 1:1,000 for IB Santa Cruz Cat#sc-17750, RRID:AB_628311
LAMTOR4 (C7orf59) (D4P6O), rabbit, used 1:500 for IF Cell Signaling Cat#13140, RRID:AB_2798129
Synaptic vesicle glycoprotein 2A (SV2), mouse, used 1:200 for IB, 1:200 for IF, 1:500 for IHC Developmental Studies Hybridoma Bank Cat#SV2, RRID:AB_2315387
TOMM20, rabbit, used 1:500 for IF, 1:200 for IB Proteintech Cat#11802-1-AP, RRID:AB_2207530
Tau-1, clone PC1C6, mouse, used 1:500 for IF Millipore Sigma Cat#MAB3420
Ankyrin-G, mouse, used 1:3 for IF NeuroMab Cat#73-146, RRID:AB_10697718
NDUFS1 (E4K3E), rabbit, used 1:100 for IB Cell Signaling Cat#70264
SDHA, mouse, used 1:100 for IB Abcam Cat#ab14715, RRID:AB_301433
CYCS (D18C7), rabbit, used 1:100 for IB Cell Signaling Cat#11940, RRID:AB_2637071
CYCS (6H2.B4), mouse, used 1:200 for IF BD Bioscience Cat#556432, RRID:AB_396416
COX IV (3E11), rabbit, used 1:100 for IB Cell Signaling Cat#4850, RRID:AB_2085424
ATP5A (15H4C4), mouse, used 1:100 for IB Abcam Cat#ab14748, RRID:AB_301447
MIC60/Mitofilin, rabbit, used 1:100 for IB Proteintech Cat#10179-1-AP, RRID:AB_2127193
MIC10/MINOS1, rabbit, used 1:100 for IB Novus Biologicals Cat#NBP1-91587, RRID:AB_11030043
LC3 (D11), rabbit, used 1:200 for IF Cell Signaling Cat#3868, RRID:AB_2137707
TGN46, sheep, used 1:1,000 for IF Bio-Rad Cat#AHP500G, RRID:AB_323104
Synapsin 1, rabbit, used 1:1,000 for IB Thermo Fisher Scientific Cat#PA1-4673, RRID:AB_561585
M6PR-CI (2G11), mouse, used 1:200 for IF Abcam Cat# ab2733, RRID:AB_2122792
EEA1(C45B10) rabbit, used 1:500 for IF Cell Signaling Cat#3288, RRID:AB_2096811
RPL24, rabbit, used 1:50 for IF Proteintech Cat# 17082-1-AP
RRID:AB_2181728
RPS27A, rabbit, used 1:50 for IF MyBioSource Cat#MBS7103451
Puromycin (12D10), mouse, 1:500 for IF Millipore Sigma Cat# MABE343
RRID:AB_2566826

Secondary antibodies:

Alexa Fluor 647-conjugated goat anti chicken IgY, used 1:1,000 for IF Thermo Fisher Scientific Cat#A-21449, RRID:AB_1500594
Alexa Fluor 555-conjugated donkey anti mouse IgG, used 1:1,000 for IF Thermo Fisher Scientific Cat#A-31570, RRID:AB_2536180
Alexa Fluor 488-conjugated donkey anti rabbit IgG, used 1:1,000 for IF Thermo Fisher Scientific Cat#A-21206, RRID:AB_2535792
Alexa Fluor 647-conjugated goat anti sheep IgG, used 1:1,000 for IF Thermo Fisher Scientific Cat#A-21448, RRID:AB_2535865
HRP-conjugated goat anti-rabbit IgG (H+L), used 1:5,000 for IF Jackson ImmunoResearch Cat#111-035-144, RRID:AB_2307391
HRP-conjugated goat anti-chicken IgY (H+L), used 1:5,000 for IF Jackson ImmunoResearch Cat#103-035-155, RRID:AB_2337381
HRP-conjugated donkey anti-mouse IgG (H+L), used 1:5,000 for IF Jackson ImmunoResearch Cat#715-035-150, RRID:AB_2340770

Validation

All antibodies are from commercially available sources and have been validated by the manufacturer with supporting publications found on manufacturer websites.
For rabbit BORCS5 (LOH12CR1): https://www.ptgcn.com/products/LOH12CR1-Antibody-17169-1-AP.htm
For rabbit BORCS7 (C10orf32): https://www.abnova.com/en-global/product/detail/pab23142
For mouse GAPDH (0411): https://www.scbt.com/p/gapdh-antibody-0411
For mouse Alpha-tubulin: https://www.scbt.com/p/alpha-tubulin-antibody-dm1a
For mouse LAMP1: https://dshb.biology.uiowa.edu/H4A3
For Rat LAMP1: https://dshb.biology.uiowa.edu/1D4B
For chicken MAP2: https://www.abcam.com/products/primary-antibodies/map2-antibody-ab5392.html
For rabbit MAP2(H-300): https://www.scbt.com/p/map-2-antibody-h-300
For mouse Synaptophysin 1 (SYP1) (D-4): https://www.scbt.com/p/syp-antibody-d-4
For rabbit LAMTOR4 (C7orf59) (D4P6O): https://www.cellsignal.com/products/primary-antibodies/lamtor4-c7orf59-d4p6o-rabbit-mab/13140
For mouse Synaptic vesicle glycoprotein 2A (SV2): https://dshb.biology.uiowa.edu/SV2
For rabbit TOMM20: https://www.ptglab.com/products/TOM20-Antibody-11802-1-AP.htm
For mouse Tau-1, clone PC1C6: https://www.sigmaaldrich.com/US/en/product/mm/mab3420
For mouse Ankyrin-G: https://www.antibodiesinc.com/products/anti-ankyrin-g-staining-antibody-n106-36-75-146
For rabbit NDUFS1 (E4K3E): https://www.cellsignal.com/products/primary-antibodies/ndufs1-e4k3e-rabbit-mab/70264
For mouse SDHA: https://www.abcam.com/products/primary-antibodies/sdha-antibody-2e3gc12fb2ae2-ab14715.html
For rabbit CYCS (D18C7): https://www.cellsignal.com/products/primary-antibodies/cytochrome-c-d18c7-rabbit-mab/11940
For mouse CYCS (6H2.B4): https://www.bdbiosciences.com/en-us/products/reagents/microscopy-imaging-reagents/immunofluorescence-reagents/purified-mouse-anti-cytochrome-c.556432
For rabbit COX IV (3E11): https://www.cellsignal.com/products/primary-antibodies/cox-iv-3e11-rabbit-mab/4850
For mouse ATP5A (15H4C4): https://www.abcam.com/products/primary-antibodies/atp5a-antibody-15h4c4-mitochondrial-marker-ab14748.html
For rabbit MIC60/Mitofilin: https://www.ptglab.com/products/IMMT-Antibody-10179-1-AP.htm
For rabbit MIC10/MINOS1: https://www.novusbio.com/products/minos1-antibody_nbp1-91587
For rabbit LC3 (D11): https://www.cellsignal.com/products/primary-antibodies/lc3b-d11-xp-rabbit-mab/3868
For sheep TGN46: https://www.bio-rad-antibodies.com/polyclonal/human-tgn46-antibody-ahp500.html?f=purified
For rabbit Synapsin 1: https://www.thermofisher.com/antibody/product/Synapsin-1-Antibody-Polyclonal/PA1-4673
For mouse M6PR-CI (2G11): https://www.abcam.com/products/primary-antibodies/m6pr-cation-independent-antibody-2g11-ab2733.html
For rabbit EEA1(C45B10): https://www.cellsignal.com/products/primary-antibodies/eea1-c45b10-rabbit-mab/3288
For rabbit RPL24: https://www.ptglab.com/products/RPL24-Antibody-17082-1-AP.htm
For rabbit RPS27A: https://www.mybiosource.com/polyclonal-human-antibody/rps27a/7103451
For mouse Puromycin (12D10): https://www.sigmaaldrich.com/US/en/product/mm/mabe343
For Alexa Fluor 647-conjugated goat anti chicken IgY: https://www.thermofisher.com/antibody/product/Goat-anti-Chicken-IgY-H-L-Secondary-Antibody-Polyclonal/A-21449
For Alexa Fluor 555-conjugated donkey anti mouse IgG: https://www.thermofisher.com/antibody/product/Donkey-anti-Mouse-IgG-H-L-Highly-Cross-Adsorbed-Secondary-Antibody-Polyclonal/A-31570
For Alexa Fluor 488-conjugated donkey anti rabbit IgG: https://www.thermofisher.com/antibody/product/Donkey-anti-Rabbit-IgG-H-L-Highly-Cross-Adsorbed-Secondary-Antibody-Polyclonal/A-21206
For Alexa Fluor 647-conjugated goat anti sheep IgG: https://www.thermofisher.com/antibody/product/Donkey-anti-Sheep-IgG-H-L-Cross-Adsorbed-Secondary-Antibody-Polyclonal/A-21448
For HRP-conjugated goat anti-rabbit IgG (H+L): https://www.jacksonimmuno.com/catalog/products/111-035-144
For HRP-conjugated goat anti-chicken IgY (H+L): https://www.jacksonimmuno.com/catalog/products/103-035-155
For HRP-conjugated donkey anti-mouse IgG (H+L): https://www.jacksonimmuno.com/catalog/products/715-035-150

Eukaryotic cell lines

Policy information about cell lines and Sex and Gender in Research

Cell line source(s)

Induced pluripotent stem cells (iPSCs) expressing the neuronal transcriptional activator neurogenin 2 (NGN2) under the control of a doxycycline-inducible promoter were obtained from Michael E. Ward lab, and generated as previously described (Wang C et al. Stem Cell Reports. 2017; 9: 1221-1233; Fernandopulle MS et al. Curr Protoc Cell Biol. 2018; 79: e51). HEK-293T cells were bought from ATCC Cat#CRL-11268.

Authentication

Specific KO mutations were confirmed by PCR amplification followed by Sanger sequencing.

Mycoplasma contamination

All cell lines tested negative for mycoplasma contamination.

Commonly misidentified lines
(See ICLAC register)

No commonly misidentified cell lines were used.

Animals and other research organisms

Policy information about studies involving animals; ARRIVE guidelines recommended for reporting animal research, and Sex and Gender in Research

Laboratory animals	All mice used in this study have C57BL/6J background. Mice used in the study were naïve and had normal health status. For timed pregnancies, we housed single male and female mice of 6 weeks of age in separate cages under a 12-h light-dark cycle. Housing conditions were maintained at ~23°C with 40-60% humidity. To time the deliveries, the female's weight was recorded, and the female was transferred overnight into the cage housing the male for no longer than 12 h. The following day, the two animals were separated, and the female was checked for the presence of plaque. If the plaque was absent, the female was transferred again to the male cage the following night. We monitored the weight of the female to determine increases over time. When the pregnancy was successful, we harvested embryos after 17 days for culture of primary cortical neurons. Neurons of mice with identical genotype and from the same litter were pooled and analyzed.
Wild animals	This study did not involve wild animals.
Reporting on sex	Embryonic harvesting of primary neurons did not take in consideration the sex of the animals because it cannot be easily determined at this developmental stage.
Field-collected samples	This study did not include samples collected from the field.
Ethics oversight	All mouse procedures were conducted following the NIH Guide for the Care and Use of Laboratory Animals, under protocol #21-021 approved by the NICHD Animal Care and Use Committee.

Note that full information on the approval of the study protocol must also be provided in the manuscript.